4-2007

Mechanochemical Mechanism for Fast Reaction of Metastable Intermolecular Composites Based on Dispersion of Liquid Metal

Valery I. Levitas
Texas Tech University, valery.levitas@ttu.edu

Blaine W. Asay
Los Alamos National Laboratory

Steven F. Son
Purdue University

Michelle Pantoya
Texas Tech University

Recommended Citation
V. I. Levitas, B. W. Asay, S. F. Son, and M. Pantoya, "Mechanochemical Mechanism for Fast Reaction of Metastable Intermolecular Composites Based on Dispersion of Liquid Metal," Journal of Applied Physics, Vol. 101(8), p. 83524-1, 2007. dx.doi.org/10.1063/1.2720182

Mechanochemical mechanism for fast reaction of metastable intermolecular composites based on dispersion of liquid metal

Valery I. Levitas, Blaine W. Asay, Steven F. Son, and Michelle Pantoya

Citation: Journal of Applied Physics **101**, 083524 (2007);
View online: https://doi.org/10.1063/1.2720182
View Table of Contents: http://aip.scitation.org/toc/jap/101/8
Published by the American Institute of Physics

Mechanochemical mechanism for fast reaction of metastable intermolecular composites based on dispersion of liquid metal

Valery I. Levitas[a)]
Department of Mechanical Engineering, Texas Tech University, Lubbock, Texas 79409

Blaine W. Asay
Los Alamos National Laboratory, Los Alamos, New Mexico 87545

Steven F. Son
School of Mechanical Engineering, Purdue University, 585 Purdue Mall, West Lafayette, Indiana 47907

Michelle Pantoya
Department of Mechanical Engineering, Texas Tech University, Lubbock, Texas 79409

(Received 22 September 2006; accepted 23 February 2007; published online 30 April 2007)

An unexpected mechanism for fast reaction of Al nanoparticles covered by a thin oxide shell during fast heating is proposed and justified theoretically and experimentally. For nanoparticles, the melting of Al occurs before the oxide fracture. The volume change due to melting induces pressures of 1–2 GPa and causes dynamic spallation of the shell. The unbalanced pressure between the Al core and the exposed surface creates an unloading wave with high tensile pressures resulting in dispersion of atomic scale liquid Al clusters. These clusters fly at high velocity and their reaction is not limited by diffusion (this is the opposite of traditional mechanisms for micron particles and for nanoparticles at slow heating). Physical parameters controlling the melt dispersion mechanism are found by our analysis. In addition to an explanation of the extremely short reaction time, the following correspondence between our theory and experiments are obtained: (a) For the particle radius below some critical value, the flame propagation rate and the ignition time delay are independent of the radius; (b) damage of the oxide shell suppresses the melt dispersion mechanism and promotes the traditional diffusive oxidation mechanism; (c) nanoflakes react more like micron size (rather than nanosize) spherical particles. The reasons why the melt dispersion mechanism cannot operate for the micron particles or slow heating of nanoparticles are determined. Methods to promote the melt dispersion mechanism, to expand it to micron particles, and to improve efficiency of energetic metastable intermolecular composites are formulated. In particular, the following could promote the melt dispersion mechanism in micron particles: (a) Increasing the temperature at which the initial oxide shell is formed; (b) creating initial porosity in the Al; (c) mixing of the Al with a material with a low (even negative) thermal expansion coefficient or with a phase transformation accompanied by a volume reduction; (d) alloying the Al to decrease the cavitation pressure; (e) mixing nano- and micron particles; and (f) introducing gasifying or explosive inclusions in any fuel and oxidizer. A similar mechanism is expected for nitridation and fluorination of Al and may also be tailored for Ti and Mg fuel. © *2007 American Institute of Physics*. [DOI: 10.1063/1.2720182]

I. INTRODUCTION

It is well-known that the reactivity of metallic particles (for example, Al, Ti, Zr, B, and Mg) strongly depends on their size. One of the ways to evaluate their reactivity is to study the combustion behavior of a mixture of metallic particles with some oxidizers (for example, MoO_3, WO_3, CuO, Cu_2O, and Fe_2O_3) or nitridizer and flourinizer (for example, fluoropolymers such as Teflon). Reactions of such mixtures (called thermites) are relatively slow but produce high temperatures. Metallic particles are covered by a thin oxide shell, and the reaction is controlled by diffusion of the oxidizer or oxygen to the metal and metal toward the oxidizer, through a growing oxide layer [Fig. 1(a)].

Metallic particles in traditional thermites are in the micron size range ($1-100\ \mu$m). When the particle diameter reduces to the nanometer range ($20-120$ nm), their reactivity increases by several orders of magnitude. Thus flame rates of $0.9-1$ km/s can be reached (see Refs. 1–4 for low density powders of $Al+MoO_3$ and $Al+Fe_2O_3$ nanocomposite powders), while for micron size thermites they are on the order of centimeters or meters per second. Ignition delay time also decreases by up to three orders of magnitude.[5] These very promising nanocomposite thermites are also commonly referred to as metastable intermolecular composites (MICs).

The order of magnitude of the reaction time and the temperature rise time can be estimated based on the measured value of pressure rise time at the reaction front which is $t_f \simeq 10\ \mu$s.[3] Such a reaction time is consistent with the data in Ref. 6. The order of magnitude for the heating rate is 10^8 K/s which is estimated as 1000 K/10 μs.

[a)]Author to whom correspondence should be addressed; electronic mail: valery.levitas@ttu.edu

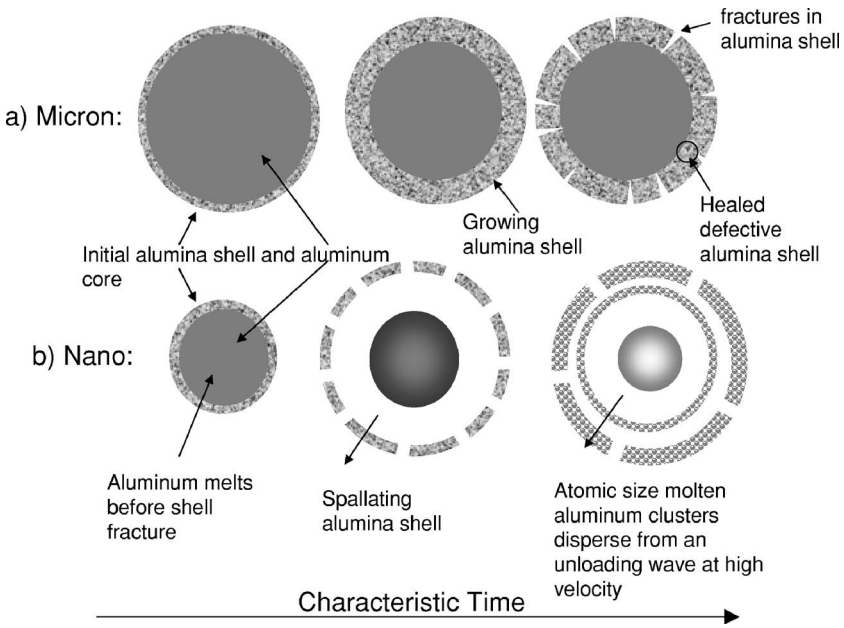

FIG. 1. (a) Micron-scale particles react by diffusion of aluminum and oxygen through an oxide shell, which fractures before Al melting and then heals. (b) Nanoscale particles during fast heating react by a melt-dispersion-mechanism where melting of the aluminum core creates enormous pressure, the oxide shell spallates exposing the molten core and creates an unloading tensile pressure wave which disperses atomic size aluminum clusters in all directions.

It is well-known that the oxidation of Al nanoparticles via a diffusion mechanism requires at least six orders of magnitude more time. The following experimental data are presented in Ref. 7: Placing the nano Al particles covered by an initial oxide shell (produced by Nanotechnologies, Inc., currently NovaCentrix, Austin, TX, the same company used in our experiments) with an average diameter of 50 nm for 1 s at a temperature of 1100 °C result in only 4% completely oxidized particles. Even keeping bare nano Al particles with an average diameter of 20 nm for 1 s at 900 °C results in only 68% completely oxidized particles. Transmission electron microscopy showed diffusive growth of the oxide shell. Since oxidation in our experiments supports flame rates up to 1 km/s without any shocks, we may assume almost complete oxidation.

Another estimate is based on the diffusion coefficients. The self-diffusion coefficient of oxygen and Al in α-alumina at 800–950 °C is at most $D=10^{-19}$ and 10^{-18} cm^2/s,[8] the diffusion length $l_d=2\sqrt{Dt_f}=(2-6)\times10^{-5}$ nm, which is 10^5 times smaller than the oxide shell thickness. Thus, the diffusion time t_f would have to be increased by a factor of 10^{10} to obtain a reasonable diffusion length $l_d=2-6$ nm. Damage of the oxide shell due to thermal stresses accelerates diffusion, however, oxidation heals cracks fast [Fig. 1(a)].

There are also other puzzles in the energetic nanocomposite materials behavior:

(1) The flame propagation rate is observed to be independent of particle size for particles diameters d smaller than 80–100 nm,[3] while for diffusion controlled oxidation it is proportional to d^{-2}.[9]
(2) The ignition time delay is found to be independent of particle size for particle diameters d smaller than 120 nm; for diffusion controlled oxidation it is a power function of diameter.[5]
(3) Nanoflakes did not produce higher flame propagation rates than micron spherical particles;[10] since they have thicknesses on the order of tens of nanometers and even larger surface to volume ratios than spherical nanoparticles, it was expected that they would posses at least similar reactivity to that of nanospherical particles.
(4) The flame propagation rate for nanothermites decreases with the sample density, while for micron size thermites it behaves oppositely.[11]

In summary, the only known reaction mechanism based on diffusion is not applicable for MICs combustion. Finding the physical mechanism of material transport and reaction for MICs is one of the most important and challenging problems in combustion physics and chemistry.

The goal of the current paper is to formulate and justify (both theoretically and experimentally) an unexpected mechanochemical reaction mechanism [Fig. 1(b)] during fast heating (10^6-10^8 K/s). This mechanism resolves the above puzzles in the combustion of MICs and allows us to predict some methods to control and improve the MICs' combustion behavior. It is known that heating creates significant internal stresses due to the difference in thermal expansion coefficients of aluminum and alumina; when Al melts, the internal stresses increase significantly due to melting-induced volume change. The small thickness of the amorphous oxide shell (1–8 nm) implies that it is (almost) defect free; so its strength approaches its maximum value equal to the theoretical (ideal) strength. It was demonstrated that for Al particles with a small ratio of particle radius to oxide thickness the alumina shell fractures after melting of the Al core, while for micrometer size particles the shell fracture precedes the core melting. The combination of a large volume change during melting and a high oxide shell strength leads to very high pressures in the Al molten core of 1–2 GPa. Fast heating and consequent pressure growth lead to the dynamic fracture of the entire alumina shell and its spallation. The complete exposure of the molten Al core with unbalanced pressure between the exposed Al surface and the internal Al droplet results in an unloading wave within the molten Al core that propagates to the particle center. An unloading wave creates a tensile pressure of the same order of magnitude that dis-

perses the molten Al particle into small (atomic scale) clusters that fly at a velocity of 100–250 m/s. The oxidation of these very small bare Al clusters is not limited by diffusion, but is rather kinetically controlled on a near atomic scale (in contrast to traditional mechanisms). If they hit the oxidizer, they will partially penetrate it, partially spread over its surface and react, and partially reflect and react with the next oxidizer particle. Aluminum clusters may react with oxygen and nitrogen in the air or with gaseous MoO_3 which starts to sublimate at 973 K.

We called these mechanochemical processes the *melt dispersion mechanism*. This mechanism produces much faster reactions than diffusion and consequently much higher flame propagation speed and heating rates for the next particles. The main conditions for operation of the melt dispersion mechanism were found, as well as parameters that control it. The main controlling parameters (for example, the ratio of particle radius to oxide shell thickness, the temperature at which initial oxide shell is formed, and the cavitation pressure) are completely unexplored for reaction and flame propagation theories. Some methods to promote the melt dispersion mechanism and expand it to micron size particles, which improves the efficiency of MICs based on the developed theory are suggested in the Introduction. Our theoretical predictions are consistent with our known experimental results and resolve the above mentioned puzzles. A similar mechanism is also expected for reactions other than oxidation, for example, fluorination and nitridation of Al. Using the found controlling parameters, the melt dispersion mechanism may be tailored for other particles (for example, for Ti and Mg particles) if they are heated very quickly to a melting temperature.

Thus, the following processes are treated in our model:

(1) Fast heating (10^6–10^8 K/s) of Al particles leading to the Al-core melting;
(2) nanomechanics of stress development in an Al particle and oxide shell;
(3) fracture and spallation of the oxide shell;
(4) unloading wave propagation to the center of a particle creating tensile pressures in the melt;
(5) cavitation and molten core dispersion.

In Sec. II, the solution of the stress determination problem in a spherical particle (consisting of a mixture of solid and liquid Al) is found and analyzed. Fracture of the oxide shell is analyzed using the maximum tensile stress criterion. It was found that for nanosize Al particle and fast heating, the major part of the Al core melts before fracture of the oxide shell, producing high pressures on the order of 1 GPa. The unloading wave created after the oxide shell spallation disperses the liquid particle. In contrast, for large particles and/or for slow heating of nanoparticles, either the oxide shell breaks before melting or slow damage to the oxide shell leads to slow flow of the liquid Al through the cracks without oxide spallation. Dependencies of the pressure within the Al core and the volume fraction of the melt necessary to fracture the oxide on the ratio of the Al particle radius, R, to the oxide thickness, δ, the temperature T_0 at which the oxide shell was formed, and the ultimate strength of the oxide, σ_u, are found; they weakly depend on the oxide thickness in the range of interest. In Sec. III, an analytical solution for the unloading and reflected wave in an Al sphere is analyzed in detail. The main features of the evolution of the tensile pressure and particle velocity distributions and their dependence of the parameters that govern the process (initial pressure and final external pressure, spallation time, particle radius, mass density, and sound speed) are found. The cavitation (fracture of liquid) criterion is formulated and the relationship between the governing parameters that lead to the cavitation and melt dispersion are determined. In Sec. IV, our previous and additional experimental data supporting our theoretical predictions and the melt dispersion mechanism are presented. In particular, the following correlations between predictions of the presented theory and experiments are obtained: (a) Extremely short reaction time; (b) for the ratio $M=R/\delta$ of the Al sphere radius to the oxide thickness below some critical value, the flame propagation rate and the ignition time delay are independent of M; (c) damage of the oxide shell suppresses the melt dispersion mechanism and promotes traditional diffusive oxidation mechanism; (d) nanoflakes react like micron size (rather than nanosize) spherical particles. Also, our experimental data are consistent with the ultimate strength of the oxide being equal to the theoretical strength of 11.33 GPa for the oxide thickness at least up to 7.7 nm. In Sec. V, the main conditions for the melt dispersion mechanism are formulated and methods of controlling and promoting this mechanism are suggested: (a) Increasing the temperature at which initial oxide shell is formed; (b) creating initial porosity in the Al; (c) mixing of Al with material with a low (even negative) thermal expansion coefficient or with a phase transformation accompanied by a volume reduction; (d) alloying Al to decrease the cavitation pressure; (e) mixing of nano- and micron particles; and (f) introducing gasifying or explosive inclusions in any fuel and oxidizer. Section VI contains the concluding remarks. In the Appendices, the main equations describing stresses in a two-layered sphere as well as thermal conductivity and wave propagation in a spherical particle are derived. Note that the first report on the melt dispersion mechanism was published in our short letter.[12] In the current paper, much more detailed theoretical and experimental justifications of the melt dispersion mechanism are presented and methods to control the mechanism are suggested.

II. INTERNAL STRESSES AND OXIDE SHELL SPALLATION

A. Small particles and fast heating

Internal stresses for a large particle covered by an oxide layer have been determined in Refs. 13 and 14. The effect of surface tension was neglected; the criterion of maximum shear stress was used, which describes well plastic flow but is not suitable for brittle fracture. Here we determine stresses for small particles (i.e., take surface tension into account), apply the criterion for brittle fracture, explore oxide thickness dependence on the strength of the shell and use our results to justify our proposed rapid oxidation mechanism. To

TABLE I. Material parameters at melting temperature $T=T_m$ (Ref. 12).

K_1^s (GPa)	K_1^m (GPa)	K_2 (GPa)	G_2 (GPa)	α_1^s (10^5 K^{-1})	α_1^m (10^5 K^{-1})	α_2 (10^5 K^{-1})	ε^m	Γ (GPa nm)	ρ_1^s (kg/m^3)	ρ_1^m (kg/m^3)
71.1	41.3	234.8	149.5	3.032	4.268	0.778	0.02	1.05	2530	2380
(Ref. 18)	(Ref. 36)	(Ref. 35)	(Ref. 35)	(Ref. 18)	(Ref. 38)	(Ref. 35)	(Ref. 14)	(Ref. 39)	(Ref. 37)	(Ref. 38)

be consistent with the fluid dynamic study in Sec. III, the compressive stresses (pressure) and consequently strains will be considered as positive.

The internal stresses that arise due to the heating of a spherical Al particle covered by the alumina oxide shell are considered. The Al particle radius by is designated by R and the external radius of the shell by $\tilde{R}=R+\delta$. The surface temperature of the particle varies from room temperature, $T_r=300$ K, to the final temperature which is just above melting temperature of Al ($T_m=933.67$ K), and corresponds to a fracture of the oxide shell; approximately, $T_f\simeq 1000$ K. This heating occurs during a time $t_f=10$ μs as the flame front passes through the particle. It is shown in Appendix A that for $R<9$ μm the temperature in the Al sphere is practically homogeneous because of the small size.

The reason for the appearance of internal stresses is a difference in inelastic strains $\varepsilon_2^i-\varepsilon_1^i$; the subscript 1 for aluminum and 2 for the alumina are used. Surface tensions at the aluminum-alumina interface, Γ_1, and between Al_2O_3 and gas that appears during the reaction (or air), Γ_2, cause jumps in pressure. They are taken into account as the boundary condition at $r=\tilde{R}$ ($p_2=2\Gamma_2/R+p_g$) and jump condition at $r=R$ ($p:=p_1=p_2+2\Gamma_1/R$), where p_g is the pressure of the gas; p_2 is the radial stress in the oxide shell; and the symbol := means "equal by definition." Displacements across the interface $r=R$ are continuous. The Al sphere consists of a mixture of melt (the volume fraction f) and solid material. Pressure in the Al sphere, p, and maximum tensile hoop stresses in the alumina oxide shell at $r=R$, σ_h, can be found from developing the corresponding solution of the elasticity theory[15] (see Appendix B)

$$p=\frac{12(m^3-1)(\varepsilon_2^i-\varepsilon_1^i)G_2K_1K_2}{H}+\frac{2K_1(4G_2+3m^3K_2)\Gamma_1}{RH}+\frac{(2\Gamma_2+p_gR)m^2K_1(4G_2+3K_2)}{RH}, \tag{1}$$

$$\sigma_h=-\frac{6(m^3+2)(\varepsilon_2^i-\varepsilon_1^i)G_2K_1K_2}{H}+\frac{4(m^3+2)G_2K_2\Gamma_1}{RH}+\frac{(2\Gamma_2+p_gR)m^2(-2G_2K_1+3(2G_2+K_1)K_2)}{RH}, \tag{2}$$

where $m=\tilde{R}/R=1+\delta/R=1+1/M$, G, and K are the shear and bulk moduli, $K_1=fK_1^m+(1-f)K_1^s$ is the bulk modulus of the Al melt-solid mixture, subscripts s and m are for the solid and melt phases, and strain $H=3m^3K_1K_2+4G_2(K_1+(m^3-1)K_2)$. Equations (1) and (2) generalize known equations found in Ref. 15 for the case when interface energy is important, i.e., for nanoparticles. Inelastic strains can be presented in the form

$$\varepsilon_1^i=-(\alpha_1^s(T_m-T_0)+(1-f)\alpha_1^s(T-T_m)+f\alpha_1^m(T-T_m)+f\varepsilon^m);$$
$$\varepsilon_2^i=-\alpha_2(T-T_0), \tag{3}$$

where α is the linear thermal expansion coefficients, T_0 is the temperature at which the oxide shell was formed on the Al particle (i.e., the temperature at which internal thermal stresses are zero), and $3\varepsilon^m$ is the volumetric expansion during the melting of Al. The first term in ε_1^i is the thermal expansion of solid Al at the melting temperature, the second and the third terms are the thermal expansion of the metastable solid phase and liquid starting with the melting temperature, and the last term is the linear expansion due to melting. Equation (3) is also correct below T_m for $f=0$ and above T_m for $f=1$. The material parameters used in calculations are presented in Table I (assuming $\Gamma_1=\Gamma_2=\Gamma$).

B. Strength criterion

We will utilize the criterion for the brittle fracture of the oxide shell: $-\sigma_h=\sigma_u$, i.e., the maximum tensile stress at the internal surface of the shell reaches the ultimate tensile strength of the oxide, σ_u. Note that in Refs. 13 and 14 the criterion of maximum shear stress, $p-\sigma_h=\sigma_u$, was used, which is not suitable for brittle fracture but rather for plastic flow. For large particles and $\delta/R\ll 1$, one obtains $p\ll|\sigma_h|$ [see Eq. (7)], i.e., the inaccuracy related to using a wrong criterion in Refs. 13 and 14 is negligible. For small particles and finite δ/R, there is a significant difference between the two criteria.

The oxide film is in an amorphous state, diffusion through the oxide, phase transformation in the oxide, and oxide growth are neglected because of the short time, $t_f=10$ μs. Ultimate tensile stress for any brittle material depends on temperature, strain rate, defects distribution, and sample size. The probability of finding defects (vacancies, voids, and cracks) in the oxide shell sharply reduces with the reduction of the oxide shell volume. For an amorphous oxide shell of $\delta=1-8$ nm, significant defects can be neglected, thus the ultimate strength by definition is equal to theoretical (maximum possible) strength of alumina, σ_{th}. High resolution transmission electron microscopy in Ref. 16 does not show significant defects, however, in Ref. 17 the oxide shell is quite porous. The defectness of the shell crucially depends on the technology of the particle synthesis process. Also, in Ref. 17 the oxide was partially amorphous and partially crystalline rather than fully amorphous. We suspect that during particle synthesis or sample preparation for transmission electron microscopy, a partial transition from amorphous to crystalline phase occurred; this transition is accompanied by an 18% volume reduction (see, for example, Refs. 19 and 20)

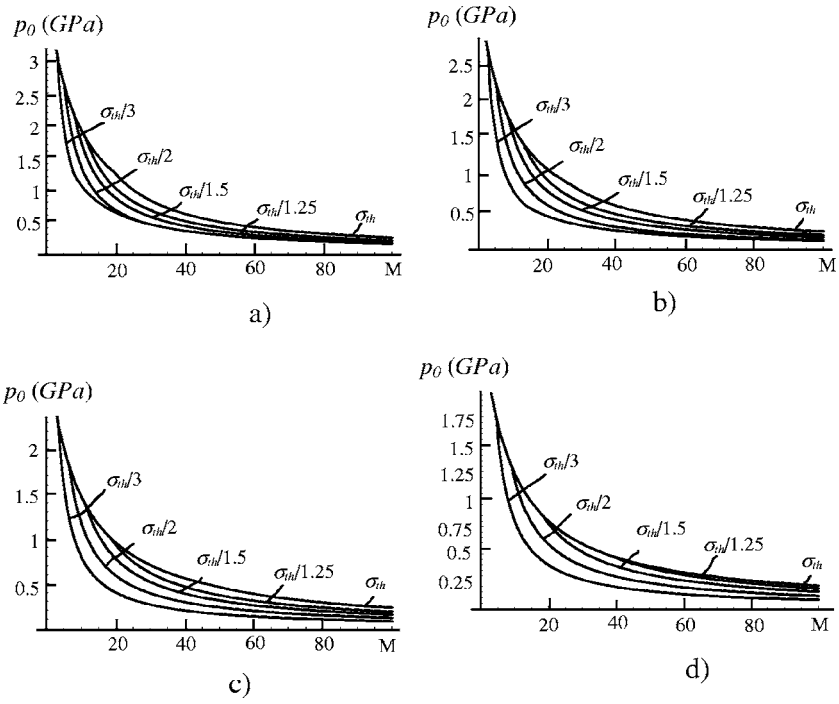

FIG. 2. Pressure p_0(GPa) in Al particle at the instant of fracture of oxide shell as a function of $M=R/\delta$ for various values of ultimate strength σ_u (shown near the curves); $\delta=2$ nm (all curves are almost independent of δ for $2<\delta<10$ nm). (a) Temperature at which initial oxide shell is formed is $T_0=300$ K; (b) $T_0=450$ K; (c) $T_0=600$ K; (d) $T_0=800$ K. The upper line common for all curves, corresponds to fracture at complete melting, $f=1$.

and huge tensile stresses (and corresponding pressure in Al core) which cause the porosity. Indeed, x-ray study of the lattice strain in Ref. 17 determined the compressive strain between (111) planes of 0.017 (which was called small). Corresponding volumetric strain is a sum of three of the same strains between three mutually orthogonal (111) planes, i.e., it is 0.051. Multiplying this strain by the Al bulk modulus at room temperature, $K=75.2$ GPa,[18] we obtain large internal pressure in Al of 3.84 GPa, which can be sustained by a porous oxide shell at room temperature and a specific loading caused by transformation in oxide.

For crystalline materials, the ideal strength is $\sigma_{\text{th}}=(1/20-1/10)E$ (Ref. 21) but to avoid an overestimate we will take $\sigma_{\text{th}}=E_2/30=11.33$ GPa, where $E_2=9K_2G_2/(3K_2+G_2)=340$ GPa is the Young's modulus (see Table I). For amorphous materials there are no such universal estimates. To be on the safe side in our predictions, we will consider much smaller oxide strength σ_u as well. We will also find in Sec. IV that $\sigma_u=\sigma_{\text{th}}$ provides the best fit to the experiments.

For $\sigma_u=E_2/30$, elastic strain $\sigma_u/E_2=1/30$ is reached during time t_f, i.e., the strain rate is very high (3.33×10^4 s^{-1}). If the oxide shell contains only a few defects, the shell's strength is lower than for the defect free case; but the defect containing shell's strength will increase with increasing strain rate significantly.[21] For very fast loading close to the theoretical strength, a fracture from pre-existing defects does not have time to propagate and homogeneous defect nucleation throughout the entire volume and spallation is the main fracture mechanism. Also, in a 2–10 nm thick shell, stress concentration due to defects in orders of magnitude smaller because of image stresses from the alumina surface. In Ref. 14 the ultimate strength of alumina was evaluated using the fracture mechanics theory. For a 1 nm long crack the ultimate strength at 660 °C was found to be 12.63 GPa which is larger than our estimate for the theoretical strength, 11.33 GPa. Molecular dynamics simulations in Refs. 22 and 23 show that the oxide shell is able to sustain an internal pressure of 1–2 GPa, which corresponds to the pressure range in this study, see Fig. 2 (despite the fact that alumina shell possessed 75% of its bulk density, i.e., had 25% voids).

Importantly, fracture and spallation occurs throughout the entire oxide shell due to the lack of significant stress concentrators and fast loading. Even at slow heating, pressures of 0.13–0.25 GPa in the melt were recorded experimentally for a thick shell before melting.[24] (We believe that the actual pressure in Ref. 24 is approximately three times higher, because linear rather than volumetric strain was used in Ref. 24 to estimate pressure.)

C. Parametric study of the oxide fracture

The tensile hoop stress σ_h in Eq. (2) grows with the increase of volume fraction of melt f. Then for some critical value of $f=f_f$, the fracture condition $-\sigma_h=\sigma_u$ is met. We obtained from Eq. (2) and from the fracture condition $-\sigma_h=\sigma_u$ the value of the volume fraction of melt, $f_f(\sigma_u,M,\delta,T_0)$, that cause the fracture of the oxide shell, where $M:=R/\delta=1/(m-1)$ (Fig. 3). We assume $p_g=0$ and that melting occurs at T_m even at such a fast heating and will use $T=T_m$ below. The high energetic solid Al-amorphous alumina interface serves as a perfect melt nucleation site (since its energy is higher than that for the liquid Al-alumina interface), so melt nucleation is barrierless. After nucleation, the solid-liquid interface propagates to the center. It continues to propagate after the fracture of the shell, however, since for small overheating the interface velocity is small in comparison with the sound velocity in Al of 4166 m/s, we will neglect this small increase in the melt volume fraction. Data on the effect of the particle size and internal pressure on the

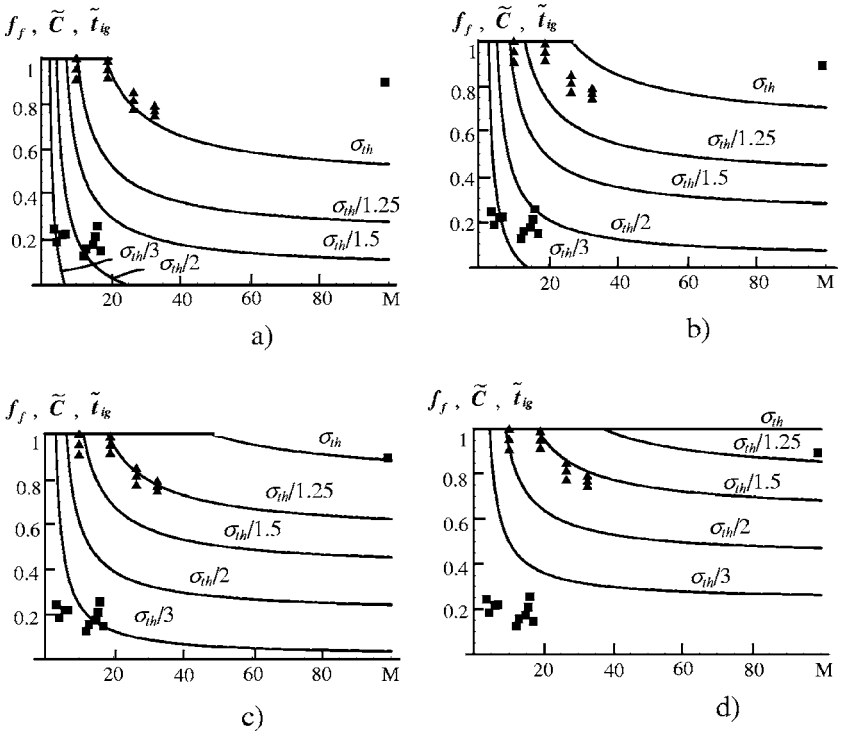

FIG. 3. Volume fraction of melt necessary for fracture of oxide shell f_f as a function of $M=R/\delta$ for various values of ultimate strength σ_u (shown near the curves); $\delta=2$ nm (all curves are almost independent of δ for $2<\delta<10$ nm). (a) $T_0=300$ K; (b) $T_0=450$ K; (a) $T_0=600$ K; (a) $T_0=800$ K. Triangles represents dimensionless flame velocity $\tilde{C}=C/(1\ \mathrm{km/s})$ versus M from experiments (Ref. 3). Squares are the relative ignition time $\tilde{t}_{ig}/(100\ \mathrm{ms})$ from experiments (Ref. 5); two other values of $\tilde{t}_{ig}$, 13.84 [for $\tilde{R}=(10-14)\ \mu$m] and 60.39 [for $\tilde{R}=20\ \mu m$] from Ref. 5 cannot be shown on the plot due to the very large values.

melting temperature are compensatory and will not be taken into account in our model. For Al nanoparticles, the melting temperature reduces with the particle size,[25] however, it simultaneously increases with internal pressure by approximately 55 K/GPa.[24] Stresses and all related parameters depend on m and (due to surface energy) on R. It is convenient to present results in terms of $M:=R/\delta$ and δ, since we found that a change in δ in a range of interest $2<\delta<10$ nm does not change significantly p, σ_h, fracture, and the function $f_f(M)$, especially for relatively large M. For example, for $T_0=600$ K and $\sigma_u=9$ GPa the following results are obtained: for $\delta=2$ nm we have $p_0=1.00$ GPa and $f_f=0.99$ (for $M=20$) and $p_0=0.50$ GPa and $f_f=0.74$ (for $M=40$); for $\delta=10$ nm we have $p_0=0.93$ GPa and $f_f=0.94$ (for $M=20$) and $p_0=0.46$ GPa and $f_f=0.72$ (for $M=40$).

Relationships $f_f(M)$ for several values of the ultimate strength σ_u and several temperatures T_0 are shown in Fig. 3. The melt concentration increases with a decrease in M (or particle radius) and with an increase in σ_u. For each value of the ultimate strength σ_u there is some critical value of M below which the melt concentration increases sharply; the smaller the σ_u the sharper the increase in the melt volume fraction. If the curve crosses the $f_f=0$ axis then fracture for larger M occurs before melting starts. The horizontal line $f_f=1$ for very small particles means that the fracture criterion is not fulfilled even at complete melting (in contrast to large particles, which fracture before melting). In this case oxide shell fracture and spallation occur during heating above the melting temperature, because thermal stresses continue to grow and the strength reduces with the temperature increase. Then, after oxide shell spallation, an unloading tensile pressure wave in the molten aluminum core disperses the entire liquid Al particle (see Sec. III). Similar phenomena occur when the major part of the Al core is molten.

Figure 3 also shows that the increase in the temperature T_0 significantly increases the volume fraction of the melt and, consequently, the probability of the occurrence of the melt dispersion mechanism.

Functions $p_0(M)$ for the pressure in the aluminum particle at the instant of the oxide shell fracture (i.e., for f determined from Fig. 3) are shown in Fig. 2 for various T_0 and σ_u. They have features that are similar to the melt concentration curves in Fig. 3. Thus, the pressure in the Al core increases with an decrease of M (or particle radius) and with an increase of σ_u. For each value of the ultimate strength σ_u there is some critical value of M below which the pressure increases sharply; the smaller σ_u the sharper the increase in pressure. The upper curve that is common for the curves with different σ_u corresponds to complete melting of Al sphere ($f_f=1$). Pressure reduces with the increasing of T_0.

For $\sigma_u=9.0$ GPa, $T_0=600$ K, and $M=20$ ($\delta=2$ nm), pressure at complete melting (which coincides with oxide shell fracture) is 1.00 GPa; reduction in σ_u reduces the value M for complete melting and even increases the pressure in Al. For comparison, for $T_0=300$ K complete melting corresponds to $M=11$ and $p=1.8$ GPa; for $T_0=800$ K we obtain $M=38$ and $p=0.53$ GPa. Consequently, our equations predict that T_0 is an important parameter controlling which the melt dispersion mechanism can be produced even for large particles.

To summarize, the melting of the major part of the aluminum nanoparticle precedes the fracture of oxide film during fast heating. Pressure in the Al core is high. After fracture and spallation of the oxide shell a tensile pressure wave disperses liquid aluminum. The smaller the relative particle size of M (above some critical value of M corresponding to com-

plete melting), the larger portion of the aluminum core melts resulting in a higher pressure in the aluminum droplet (Figs. 2 and 3).

D. Large particles and slow heating

Since we consider a thin alumina layer it follows that $\delta \ll R$ and $m-1=\delta/R \ll 1$; we expand p and σ_h [Eqs. (1) and (2)] in the Taylor series in $m-1$:

$$p=\frac{36(\varepsilon_2^i-\varepsilon_1^i)G_2K_1K_2(m-1)}{H_s}+\frac{2(\Gamma_1+\Gamma_2)}{R}+p_g, \tag{4}$$

$$\sigma_h=-\frac{18(\varepsilon_2^i-\varepsilon_1^i)G_2K_1K_2}{H_s}+\frac{12\Gamma_1G_2K_2}{RH_s}+\frac{(2\Gamma_2+p_gR)(3(2G_2+K_1)K_2-2G_2K_1)}{RH_s},$$
$$H_s=K_1(3K_2+4G_2). \tag{5}$$

The main term in σ_h is independent of m. For pressure p, the term related to surface energies is also independent of m, while the term related to $\varepsilon_2^i-\varepsilon_1^i$ is linear in $m-1$. Thus, for large particles the pressure is much smaller than the hoop stresses in a thin shell, while for nanoparticles they are comparable. Note that the first term in p is equal to the first term in σ_h multiplied by a factor of $-2\delta/R$.

For $\delta=2$ nm and $R>20$ nm the term with the surface energies in Eq. (2) for σ_h at $T=930$ K and $T_0=300$ K (without the melting of aluminum) reduces σ_h by less than 5.5%. For a higher temperature, as well as during the melting of Al and for larger R, the contribution of surface energy is negligible. Since $\sigma_u \gg p_g$, p_g can be removed from the equation for σ_h for any R and δ. The contribution of the surface energy to the pressure increase for $\delta=2$ nm, $T=930$ K, and $T_0=300$ K (without the melting of aluminum) is about 9% for $R>14$ nm and is significant for smaller particles. However, since for large particles $p \ll -\sigma_h$ and we will be interested in high T_0, we have to retain for p the terms containing the surface energies and the gas pressures

$$\sigma_h=-\frac{18G_2K_2(\varepsilon_2^i-\varepsilon_1^i)}{4G_2+3K_2}=-\sigma_u, \tag{6}$$

$$p=-2\sigma_h\frac{\delta}{R}+\frac{2(\Gamma_1+\Gamma_2)}{R}+p_g$$
$$=2\sigma_u\frac{\delta}{R}+\frac{2(\Gamma_1+\Gamma_2)}{R}+p_g \ll \sigma_u. \tag{7}$$

Since σ_h is independent of K_1 and geometric parameters, the fracture of the oxide film for relatively large Al particles is, in the first approximation, independent of mechanical properties of the spherical particle, interface energy and geometric parameters.

Substituting Eq. (3) into fracture criterion Eq. (6) and solving for the volume fraction of melt that causes fracture, we obtain

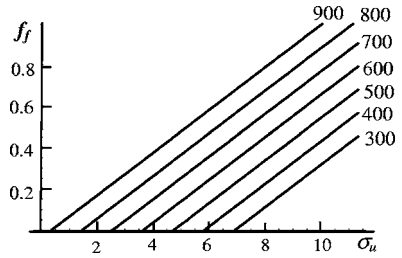

FIG. 4. Volume fraction of melt necessary for fracture of oxide shell f_f vs ultimate strength σ_u for various temperatures T_0 (shown near the curves).

$$f_f=\frac{J\sigma_u+(\alpha_2-\alpha_1^s)(T-T_0)}{\varepsilon^m+(\alpha_1^m-\alpha_1^s)(T-T_m)}, \tag{8}$$

where $J=(4G_2+3K_2)/18G_2K_2=0.0021$ for the elastic constants from Table I; Eq. (8) is independent of geometric parameters. For $T=T_m$ and all material parameters from Table I, Eq. (8) simplifies to

$$f_f=-1.052+0.103\sigma_u+0.001\,127T_0. \tag{9}$$

Function f_f versus σ_u for various temperatures T_0 are presented in Fig. 4.

Let us consider the reasons why melt dispersion should not occur during slow heating and for large particles.

(1) For $\sigma_u=11.33$ GPa and $R/\delta=2000$, we obtain from Eq. (7) $p_0-p_g=11.5$ MPa which may not produce sufficient tensile stress in the unloading wave to disperse the solid aluminum core. For $\sigma_u=11.33$ GPa and $T_0=300$ K, we obtain from Eq. (9), $f_f=0.45$ only.

(2) If melting of an Al nanoparticle covered by an amorphous film occurs during slow heating,[26] low stress (strain) growth rate takes place. This will reduce the ultimate strength of the thick defect-containing oxide film (due to strong strain rate dependence) and the pressure in the particle.

(3) For slow heating and, consequently, slow loading, fracture will occur in the weakest point of the oxide at the interface with Al (rather than in the whole oxide film) and then it will propagate toward the external oxide boundary. Pressure in molten aluminum will also slowly reduce and the liquid will slowly flow through the cracks without spallation and thus dispersion of the entire film and Al as observed experimentally.[26] Melt will be quickly covered by a new oxide film. There is some acceleration of oxidation during this process followed by traditional diffusion-controlled mechanisms for further oxidation. These results are in qualitative agreement with experiments in Ref. 26 on oxide fracture of Al nanoparticles due to the melting of Al during relatively slow heating. As it will be shown in Sec. III, time during which the oxide shell fracture occurs is an important parameter to create tensile pressure in the molten Al: It has to be very short, on the order of 10 ps.

(4) During slow heating and when oxide thickness exceeds the critical value of $\simeq 4$ nm (initially or during its growth), a phase transformation of amorphous into γ crystalline phase occurs in the Al_2O_3. For example, for the heating rate of 5–10 K/min of micrometer size particles it occurs at $T \simeq 820$ K (Refs. 19 and 20) (much below the Al

melting temperature). A huge volumetric compression during this transformation (0.1818, i.e., three times larger than for the melting of Al) produces tensile hoop stresses approximately three times larger than during melting. Also, polycrystalline γ phase contains traditional defects (grain boundaries and dislocations) which reduce the ultimate tensile strength by up to several orders of magnitude in comparison with σ_{th}. The combination of high stresses and lower strength will result in the oxide fracturing at an earlier stage of transformation, as is observed in experiments[19,20] and follows from Eqs. (1) and (2). Oxide fracture during the transformation in alumina leads to accelerated oxidation of the bare Al until it is covered by the γ phase film.

Note that we neglected this transformation for fast heating because of the very short time t_f (as well as in some cases because of $\delta<4$ nm). Based on kinetic data in Ref. 27 complete transformation time at T_m is 200 s, therefore, even for a heating time of 2 s up to T_m phase transformation can be completely neglected even for thick shells.

After phase transformation and healing of the oxide film, further heating above the melting temperature will result in a jump in inelastic strains given by Eq. (3) with $T_0 \simeq 820$ K, i.e., in lower internal stresses than we calculated in Fig. 1. This could be favorable for increasing f_f, causing the next fracture of the film [see discussion after Eq. (8)]. However, since the oxide layer is much thicker at the Al melting point than during the phase transformation in alumina (20 nm versus 4 nm),[19,20] and pressure grows slowly with the increase of f, damage (nanocracks) can be initiated at the aluminum-alumina interface (where the hoop stresses are the largest) and slowly propagate to the external radius of the particle. Liquid aluminum fills these nanocracks. This leads to the reduction of the Al mass within the sphere of the initial radius R, reduction of internal pressure, and slowing (arresting) the damage. Nanocracking introduces tensile volumetric stress in alumina thus decreasing $\varepsilon_2^i-\varepsilon_1^i$ and stresses. Also, oxygen can more easily reach the thin layers of liquid Al in cracks and cause Al oxidation. This not only leads to the healing of the alumina film but also introduces additional tensile volumetric inelastic strain, again reducing pressure in Al and hoop stresses.

(5) An additional reason that may prevent the oxide fracture below Al melting during slow heating of relatively large particles is the outward diffusion of Al cations through the oxide which represents the major mechanism of the oxide film growth.[19,20] Such a mass transport reduces the volume and pressure in the Al liquid particle. Indeed, there are no observations of acceleration of oxidation after Al melting ($T>T_m$) in Refs. 19 and 20 and consequently no additional fracture due to melting is expected.

(6) During fast heating allow the fracture of large particles to occur before melting (before or after the phase transformation in alumina) and the oxide shell be healed (or a new shell appear) at $T_0<T_m$. This is equivalent to an increase in T_0 and may lead to melting before the next fracture. If such a regime can be realized in practice, it will significantly increase the particle size for which the melt dispersion mechanism is operative. However, some events can prevent it. The oxide shell can be very defective and consequently possess low strength. Indeed, in the production of nanoparticles, one needs to use very specific parameters (temperature and oxygen content and their rate of change, as well as exposure time) to obtain a hard, defect-free (or almost defect free) oxide of homogeneous thickness. Healing of oxide film under nonoptimal conditions leads to the presence of defects (vacancies and voids), i.e., to damage. Also, new shells may be too thin at the fracture instant yielding inadequate pressure in the melt. Alternatively, fast oxidation of bare Al causes surface melting and the appearance of a thick defective oxide (amorphous or crystalline) shell which also breaks at low pressures. Much more detail and precise modeling is required to tailor this process.

III. WAVE PROPAGATION AND DISPERSION OF LIQUID IN AN UNLOADING WAVE

A. Problem formulation

We consider a sphere of radius R that is initially in equilibrium under applied external pressure p_0. Let the pressure at the boundary $r=R$, $p_{\text{ex}}(t)$, reduce linearly in time from p_0 to the final value p_f during the time of oxide shell spallation, t_s, after which it remains constant, i.e.,

$$p_{\text{ex}}(t)=(p_0-(p_0-p_f)t/t_s)U(0,t_s)+p_fU(t_s,t), \tag{10}$$

where $U(a,b)=H(\alpha-a)H(b-\alpha)$ is the unit step function on the interval $[a,b]$ [that is $U(a,b)=1$ on the interval $[a,b]$ and 0 outside $[a,b]$], and H is the Heaviside unit step function (i.e., $H(\alpha-a)=1$ for $\alpha\geq a$ and 0 for $\alpha<a$). Let $c=\sqrt{K/\rho}$ be the sound velocity, where ρ is the mass density. It is useful to define an acoustic time $t_p=R/c$; during this time changes at the particle boundary reach the center of the sphere. We normalize length, time, and pressure by R, t_p, and p_0 respectively; all normalized parameters will be designated by a bar. Then Eq. (10) can be presented in the form

$$\begin{aligned} p_{\text{ex}}(t)&=p_0\bar{p}_{\text{ex}}(\bar{t})\\ &=p_0[(1-(1-\bar{p}_f)\bar{t}/\bar{t}_s)U(0,\bar{t}_s)+\bar{p}_fU(\bar{t}_s,\bar{t})]. \end{aligned} \tag{11}$$

The sound velocity in liquid Al is $c=\sqrt{K_1^m/\rho_1^m}=4166$ m/s, where K_1^m and ρ_1^m are taken from Table I. Consequently, for $R=41.66$ nm the acoustic time is $t_p=10$ ps. Molecular dynamics simulations in Refs. 22 and 23 show that the formation time of the oxide shell on a bare Al surface occurs in approximately 20 ps. That is why we will consider unloading and the first reflected wave only. For rapid heating of an aluminum nanoparticle covered by a thin oxide film when the fracture of the shell occurs at the theoretical strength, we have $t_s\ll t_p$. Indeed, even if we consider crack propagation through the oxide shell under intense loading (which takes longer than a simultaneous fracture of the whole oxide shell), the velocity of crack propagation is of the same order of magnitude as the sound speed in alumina, c_a, and $t_s\simeq\delta/c_a\ll t_p$, because $\delta\ll R$ and $c_a>c$. To be conservative, we take $t_s=0.2t_p$ as a reasonable estimate. The gas pressure which develops during the flame propagation can be estimated as 0.01 GPa. Maximum gas pressure in Ref. 3 (corresponding to a maximum temperature of several thousand K) for a high propagation velocity regime was recorded to be

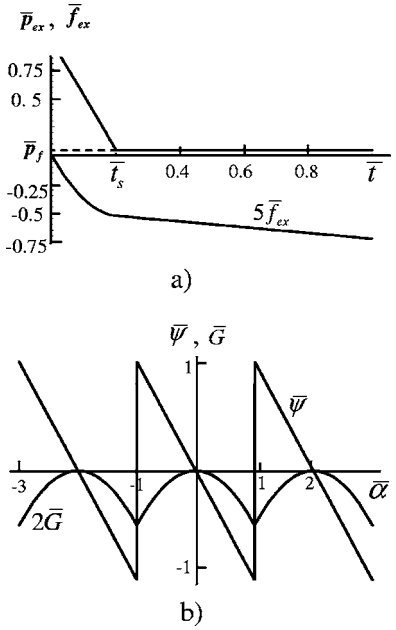

FIG. 5. Functions $\bar{p}_{ex}(\bar{t})$, $\bar{f}_{ex}(\bar{t})$, $\bar{\Psi}(\bar{\alpha})$, and $\bar{G}(\bar{\alpha})$ used in the solution of the wave propagation problem.

0.018 GPa, however, at melting temperatures it should be much lower. For $\sigma_u=11.33$ GPa, $\delta=2$ nm, and $R=50$ nm, p_0 varies between 1 and 2 GPa [Fig. 2(a)] and $p_f=2\Gamma/R+p_g\simeq 0.05$ GPa. The fracture of liquid (cavitation) criterion is $p<p_c<0$, where p_c is the critical tensile pressure; we can estimate $p_c=-0.01$ to -1 GPa (see below).

B. Analytical solution

We found analytically the pressure and particle velocity evolutions during such a loading (see Appendix C):

$$p=\frac{p_0}{\bar{r}}\left[-\frac{1}{2}(\bar{\Psi}(\bar{r}+\bar{t})+\bar{\Psi}(\bar{r}-\bar{t}))+\bar{p}_{ex}(\bar{t}+\bar{r}-1)-\bar{p}_{ex}(\bar{t}-\bar{r}-1)\right], \tag{12}$$

$$v=\frac{p_0}{\rho c\bar{r}}\left[\frac{1}{2}(\bar{\Psi}(\bar{r}+\bar{t})-\bar{\Psi}(\bar{r}-\bar{t}))-(\bar{p}_{ex}(\bar{r}+\bar{t}-1)+\bar{p}_{ex}(\bar{r}-\bar{t}-1))-\frac{\bar{f}_h+\bar{f}_b}{\bar{r}}\right], \tag{13}$$

where functions $\bar{\Psi}$, $\bar{p}_{ex}$, $\bar{f}_h$, and $\bar{f}_b$ are given in Appendix C and in Fig. 5.

Thus, pressure and particle velocity fields scale with p_0 and $p_0/\rho c=p_0/\sqrt{K\rho}$, respectively; they depend on dimensionless parameters $\bar{p}_f$ and $\bar{t}_s$. It is important that the pressure and velocity do not explicitly depend on the particle size R; thus wave propagation does not limit the validity of the melt dispersion mechanism to nanoparticles only. Allowing for nonlinear elasticity of the melt reduces the sound velocity c and increases the particle velocity without changing the pressure. We will study the effect of the parameters $\bar{p}_f$ and $\bar{t}_s$ on the pressure and velocity fields.

Below we will present results for $p_0=1$ GPa and the above values of K_1^m, ρ_1^m, and c, i.e., for $p_0/p_0=100.86$ m/s. Rescaling can be produced using Eqs. (12) and (13).

The results on pressure and particle velocity during the wave propagation are shown in Fig. 6 for $\bar{t}_s=0.2$ and $\bar{p}_f=0.05$. Pressure p_h (see Appendix C) immediately jumps into the tensile (negative) region near the boundary and the tensile region propagates to the center with the sound velocity c, increasing in magnitude. However, the total pressure p is compressive at least until $\bar{t}\simeq\bar{t}_s$, when the region with $p=p_f$ starts to propagate from the external surface of the sphere. For the time in the range $\bar{t}_s<\bar{t}<\bar{t}_p$, the region with tensile pressure p appears and propagates to the center of the particle; the growth in the magnitude of tensile pressure is significant (Fig. 6). The maximum tensile pressure and radial velocity correspond to the point $\bar{r}=1+\bar{t}_s-\bar{t}$ which is reached by the minimum pressure $(\bar{p}_f)$ point of the propagating boundary regime. Radial particle velocities during propagation are positive (i.e., from the center). For $\bar{t}=1$, the maximum values of tensile pressure and velocity in the central part of the particle are as high as $|p|=3.75$ GPa and $v=240$ m/s, respectively.

The tensile pressure in the central part of an Al particle continues to grow at the initial stage of wave reflection, for $\bar{t}\le 1+0.5\bar{t}_s$. Thus, for $\bar{t}=1.1$, the absolute value of the tensile pressure distribution reaches its maximum. The tensile pressure at the center is 8.5 GPa, however, velocity is zero everywhere, and no dispersion can occur. For $\bar{t}>1.1$ velocity becomes negative or zero everywhere, which also cannot cause dispersion. However, for $1<\bar{t}<1.1$ there is still a region where both negative pressure and positive velocity are high and can cause melt dispersion (if that did not occur as a result of $\bar{t}<1$). Thus, the melt dispersion criterion is not only $p<p_c$ (see below) but also $v>0$.

For $\bar{t}_s=0.5$ and $\bar{p}_f=0.05$, the evolution of the pressure and particle velocity distributions are presented in Fig. 7. It is qualitatively similar to the case with $\bar{t}_s=0.2$ but with smaller magnitude of maximum tensile pressure and velocity. Thus, for $\bar{t}=1$, the maximum tensile pressure and velocity in the central part of a sphere are $|p|=0.90$ GPa and $v=96$ m/s, respectively. The maximum tensile pressure in the reflected wave is $|p|=2.80$ GPa. For $\bar{t}=1.25$ the velocity is zero everywhere, for larger $\bar{t}$ it becomes negative or zero everywhere.

For the same conditions, however, for $\bar{t}_s=1$ there is no tensile pressure in the sphere for $\bar{t}<1$. The results in Fig. 8 are presented for the reflected wave, $1\le\bar{t}\le 1.5$. During the initial stage of propagation of the reflected wave, tensile pressure appears with a maximum amplitude of 0.90 GPa near the center. The fracture criterion $p<p_c=-0.1$ GPa is satisfied in the major internal part of the drop $(\bar{r}<0.86)$. Velocity in the region of constant tensile pressure is zero, but increases up to 48 m/s with decreasing r. The dispersion of liquid droplets is still possible, but with smaller velocity. If, however, there is some delay time for the fracture of liquid, e.g., $\bar{t}_d=0.1-0.5$ depending on pressure, this practically will not affect melt dispersion for $\bar{t}_s=0.2$ and $\bar{t}_s=0.5$ but will make melt dispersion impossible for $\bar{t}_s=1$. Indeed, the time between the appearance of tensile pressure and the violation

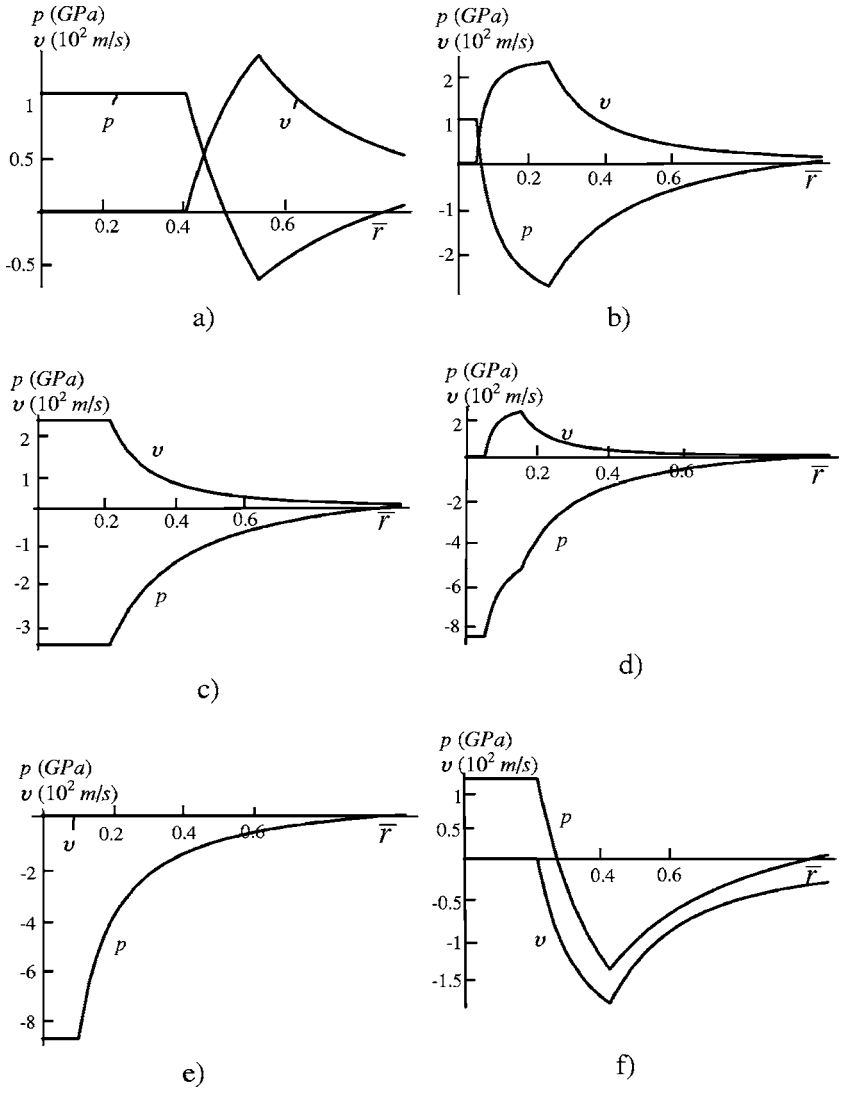

FIG. 6. Pressure (GPa) and particle velocity (10^2 m/s) distributions in Al sphere after spallation of oxide shell at different instants of propagation of the unloading (a)–(c) and reflected (d)–(f) waves for $\bar{t}_s=0.2$, $p_0=1$ GPa, and $\bar{p}_f=0.05$: (a) $\bar{t}=0.6$; (b) $\bar{t}=0.95$; (c) $\bar{t}=1$; (d) $\bar{t}=1.05$; (e) $\bar{t}=1.1$, and (f) $\bar{t}=1.4$. Maximum positive velocity corresponds to $\bar{t}=1$; maximum tensile pressure corresponds to $\bar{t}=1.1$ when velocity is zero everywhere. For $\bar{t}>1.1$ the velocity is negative (to the center), i.e., melt dispersion (if would not occur for $\bar{t}<1.1$) is getting impossible.

the condition $v>0$ is less than $0.5t_p$ and if we take $\bar{t}_d=0.5$ (because of small tensile pressure) then dispersion criterion will not be satisfied. Since t_d is independent of t_p, if the radius of Al sphere increases, t_p increases, $\bar{t}_d$ decreases, and there are more chances that melt dispersion will occur (provided that the oxide breaks fast at $-\sigma_h=\sigma_u$ and that the pressure in the Al is high enough). At $\bar{t}=1.5$ the velocity is zero everywhere and for larger $\bar{t}$ it becomes negative everywhere.

For $\bar{t}_s=1.5$, the situation is qualitatively similar to the case of $\bar{t}_s=1$ (Fig. 9), i.e., tensile pressure in the Al appears in reflected wave only. The maximum tensile pressure and velocity reach 0.27 GPa and 32 m/s, respectively. The fracture criterion $p<p_c=-0.1$ GPa and $v>0$ is satisfied at each time instant $1<\bar{t}<1.75$ in a small moving layer only. At $\bar{t}=1.75$ the velocity is zero everywhere and for larger $\bar{t}$ it becomes negative everywhere. For $\bar{t}_s\geq 1.9$, tensile pressure does not appear in the first unloading and reflected waves, so dispersion is impossible.

C. Some general features

Let us study some general features of the effect of the time of the pressure drop, $\bar{t}_s$, and the pressure on the Al sphere after the oxide shell is broken, $\bar{p}_f$, on the pressure and particle velocity distributions. The following general results are obtained for any $\bar{p}_f<1$. The maximum tensile pressure distribution corresponds to $\bar{t}=1+0.5\bar{t}_s$, when velocity is identically zero within the sphere. For $\bar{t}=1$, velocity in the central part reaches its maximum value, which is found to be

$$v_m=\frac{p_0}{2\rho c}\frac{(1-\bar{p}_f)}{\bar{t}_s}, \tag{14}$$

for the above accepted values of ρ, c, and $p_0=1$ GPa, it is $v_m=50.432(1-\bar{p}_f)/\bar{t}_s$(m/s). In Fig. 10, pressure distributions at $\bar{t}=1$ and $\bar{t}=1+0.5\bar{t}_s$, as well as velocity distributions at $\bar{t}=1$ are shown for various $\bar{t}_s$ and $\bar{p}_f=0.05$; results for other $\bar{p}_f$ are configurationally similar. Several important results can be derived from this study. For $\bar{t}=1+0.5\bar{t}_s$ and in the region $0\leq\bar{r}\leq 0.5\bar{t}_s$, pressure is constant and is equal to the maximum tensile pressure

$$\bar{p}_{\max}=1-2(1-\bar{p}_f)/\bar{t}_s. \tag{15}$$

For $\bar{t}=1$ and in the region $0\leq\bar{r}\leq\bar{t}_s$, the velocity and tensile pressure are constant and equal to their maximum values, v_m [Eq. (14)] and

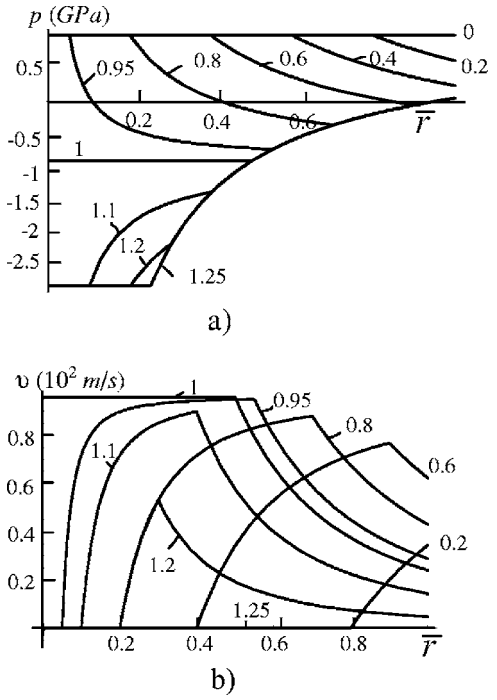

FIG. 7. Pressure [(a), in GPa] and particle velocity [(b), in 10^2 m/s] distributions in Al sphere after spallation of oxide shell at different instants $\bar{t}$ (shown near the curves) of waves propagation for $\bar{t}_s=0.5$, $p_0=1$ GPa, and $\bar{p}_f=0.05$. For the pressure plots, the upper line ($\bar{t}=0$ and $p=1$ GPa) and the lowest curve (for $\bar{t}=1.25$) are common for all curves for $\bar{t}\leq 1$, i.e., at each time the pressure profile consists of straight horizontal line (1 GPa) in the central part, the line connecting to the lowest curve and part of the lowest curve. In the reflected pressure wave, the pressure profile for $1<\bar{t}<1.25$ deviates from the lowest curve in some internal layer only. For $\bar{t}=1.25$ the velocity is zero everywhere and getting negative for $\bar{t}>1.25$ (not shown).

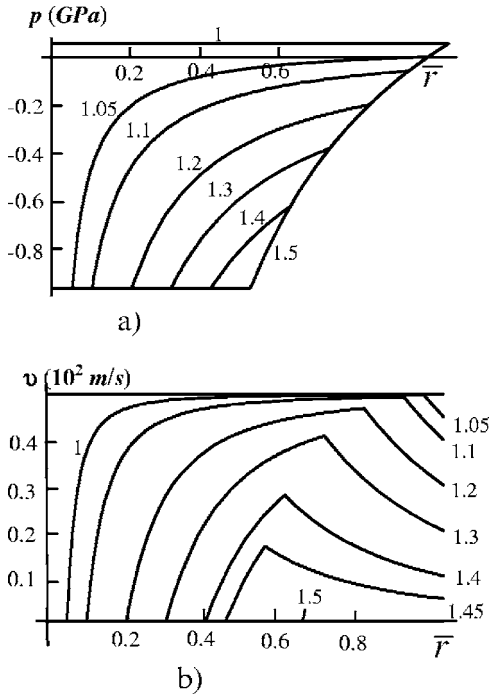

FIG. 8. Pressure [(a), in GPa] and particle velocity [(b), in 10^2 m/s] distributions in Al sphere after spallation of oxide shell at different instants $\bar{t}$ (shown near the curves) of reflection wave propagation for $\bar{t}_s=1$, $p_0=1$ GPa, and $\bar{p}_f=0.05$. The pressure profiles for $1<\bar{t}<1.5$ deviates from the lowest curve (for $\bar{t}=1.5$) in some internal layer only. For $\bar{t}=1.5$ the velocity is zero everywhere and getting negative for $\bar{t}>1.5$ (not shown).

$$\bar{p}_m = 1-(1-\bar{p}_f)/\bar{t}_s. \tag{16}$$

The deviation from 1 for $\bar{p}_m$ is two times smaller than for $\bar{p}_{\max}$. The magnitudes of $\bar{p}_m$ and $\bar{p}_{\max}$ in the tensile region linearly reduce with the growth of $\bar{p}_f$ and decreases in inverse proportion with the increase in $\bar{t}_s$. These pressures are tensile if $\bar{t}_s<2(1-\bar{p}_f)$ (for $\bar{p}_{\max}$) and $\bar{t}_s<(1-\bar{p}_f)$ (for $\bar{p}_m$). For $\bar{p}_f=1$ one gets $\bar{p}_{\max}=\bar{p}_m=1$.

The pressure distribution for $\bar{t}=1$ (in addition to the above constant part) coincides in the region $\bar{t}_s\leq\bar{r}\leq 1$ with the distribution for $\bar{t}=1+0.5\bar{t}_s$. The tensile pressure distribution curve for any $\bar{t}_s<\bar{t}<1+0.5\bar{t}_s$ and for $\bar{r}$ greater than some value consists of the portion of the pressure curve for $\bar{t}=1+0.5\bar{t}_s$; for $1<\bar{t}<1+0.5\bar{t}_s$ these curves coincide in some central part of a sphere as well (Figs. 6–9).

The most important point that follows from Fig. 10 is that the pressure distribution in some external region of the sphere is independent of $\bar{t}_s$. For $\bar{t}=1+0.5\bar{t}_s$, all pressure distributions for various $\bar{t}_s$ coincide in the region $0.5\bar{t}_s\leq\bar{r}\leq 1$; for $\bar{t}=1$, all pressure distributions for different $\bar{t}_s$ coincide in the region $\bar{t}_s\leq\bar{r}\leq 1$. Combining this result with the previous results on a wave propagation along the radius (Figs. 6–9), we can conclude that for any time $\bar{t}_s<\bar{t}<1+0.5\bar{t}_s$, pressure distribution in the region $1+\bar{t}_s-\bar{t}\leq\bar{r}\leq 1$ is the same, independent of $\bar{t}$ and the parameter $\bar{t}_s$. It was found to be described by the following equation:

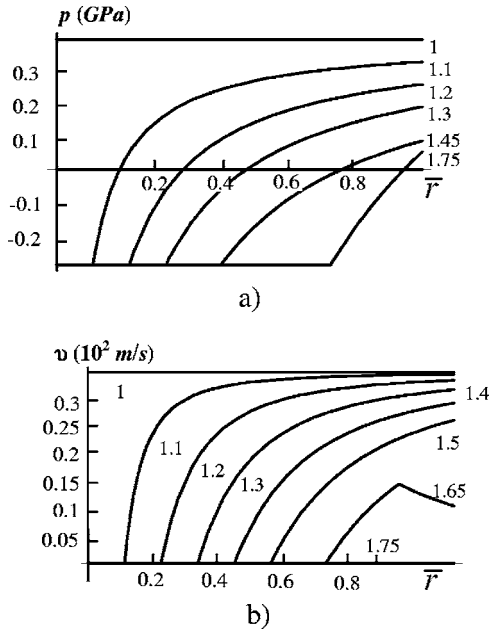

FIG. 9. Pressure [(a), in GPa] and particle velocity [(b), in 10^2 m/s] distributions in Al sphere after spallation of oxide shell at different instants $\bar{t}$ (shown near the curves) of reflection wave propagation for $\bar{t}_s=1.5$, $p_0=1$ GPa, and $\bar{p}_f=0.05$. The all pressure profiles for $1<\bar{t}<1.75$ reach the maximum tensile pressure of 0.27 GPa in the central region of the sphere. The fracture criterion $p<p_c=-0.1$ GPa and $v>0$ is satisfied at each time instant $1<\bar{t}<1.75$ in a small moving layer only. At $\bar{t}=1.75$ velocity is zero everywhere and for larger $\bar{t}$ it is getting negative everywhere (not shown).

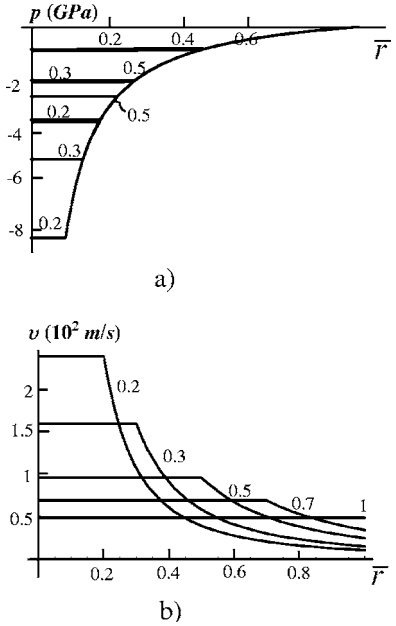

FIG. 10. Pressure [(a), in GPa] and particle velocity [(b), in 10^2 m/s] distributions in Al sphere after spallation of oxide shell at instants $\bar{t}=1$ [bold lines in (a)] and $\bar{t}=1+0.5\bar{t}_s$ for $p_0=1$ GPa, $\bar{p}_f=0.05$, and various $\bar{t}_s$ (shown near the curves). Pressure distribution for $\bar{t}=1$ coincides with the distribution for $\bar{t}=1+0.5\bar{t}_s$ for $\bar{t}_s\le\bar{r}\le 1$ for any $\bar{t}_s$. More generally, for any time $\bar{t}_s<\bar{t}<1+0.5\bar{t}_s$, pressure distribution in the region $1+\bar{t}_s-\bar{t}\le\bar{r}\le 1$ is the same independent of $\bar{t}$ and the parameter $\bar{t}_s$.

$$\bar{p}(\bar{r})=1-\frac{1-\bar{p}_f}{\bar{r}}. \tag{17}$$

At the boundary of the region where this equation is valid, for $\bar{r}=\bar{r}_m:=1+\bar{t}_s-\bar{t}$ (this point is reached by the constant pressure portion, $\bar{p}_f$, of the propagating boundary regime), pressure reaches its maximum tensile value

$$\bar{p}_m(\bar{t})=1-\frac{1-\bar{p}_f}{1+\bar{t}_s-\bar{t}}. \tag{18}$$

For $\bar{t}=1$ and $\bar{t}=1+0.5\bar{t}_s$, Eq. (18) gives the same pressure as Eqs. (16) and (15).

There is an important practical conclusion that follows from this result. If we limit ourselves with the condition $\bar{t}\le 1$ (when the particle velocity is directed from the center), then if the maximum pressure in the central part of the sphere at $\bar{t}=1$, $\bar{p}_m$ [Eq. (16)], is smaller than the critical pressure for cavitation ($\bar{p}_m<\bar{p}_c:=p_c/p_0<0$), then the cavitation criterion

$$\bar{p}(\bar{r})=1-\frac{1-\bar{p}_f}{\bar{r}}=\bar{p}_c, \tag{19}$$

is met in the same region of the sphere independent of $\bar{t}_s$, namely for

$$\bar{r}\le\bar{r}_m\frac{1-\bar{p}_f}{1-\bar{p}_c}. \tag{20}$$

Still, the condition $\bar{p}_m<\bar{p}_c$ limits the spallation time

$$\bar{t}_s\le\frac{1-\bar{p}_f}{1-\bar{p}_c}. \tag{21}$$

Coincidence of inequalities for $\bar{r}$ and $\bar{t}_s$ is not accidental. For $\bar{t}=1$ the equation $\bar{r}_m=1+\bar{t}_s-\bar{t}$ (at this point tensile pressure reaches its maximum) results in $\bar{r}_m=\bar{t}_s$.

Note that for $\bar{t}>1+0.5\bar{t}_s$, the velocity becomes zero at the central part of the sphere and negative in its remaining part. For $\bar{t}_s\ge 1$ and $\bar{t}=1$, the pressure and velocity are homogeneous but the pressure is compressive. For $\bar{p}_f=1$ one has $\bar{p}=1$ and $\upsilon=0$.

D. Cavitation in liquid aluminum

The fracture of liquid (cavitation) can be considered a nucleation problem.[28] The radius of the critical nucleus for homogeneous nucleation, $r_{cr}=2\Gamma/|p|$, for $|p|=1.05$ GPa is 2 nm, which is reasonable, but for $|p|=0.105$ GPa it is 20 nm which is comparable to the Al particle radius and is unrealistic. Thus the theoretical value of the critical tensile pressure to cause the fracture of liquid Al is $p_c\simeq -1$ GPa. However, the actual pressure at which cavitation occurs may be several orders of magnitude smaller (this is similar to the actual strength in comparison with the theoretical strength for solids). This happens for various reasons, such as the existence of nanovoids, impurities, or solute atoms that reduce the local value of Γ. For example, for water at room temperature ($\Gamma_w=0.08$ GPa nm), $r_{cr}=2$ nm corresponds to $|p_c|=76$ MPa while cavitation is observed at the pressure range from 0.2 MPa to several MPa.[28] Aluminum nanoparticles contain the B, H, water, Fe, Cu, K, and N impurities.[17] Thus, we also will consider $|p_c|$ in the range 0.01–1 GPa. For $p_c=-0.1$ GPa, the fracture criterion, $p<p_c$, is satisfied at radius $\bar{r}_f=0.86$ (Figs. 6–8 and 10).

Cavitation causes the separation of a thin liquid outer shell from the main spherical droplet. When the liquid shell is separated from the Al particle, its thickness, $\tilde{\delta}(t)$, becomes thinner while its internal radius, $r(t)$, grows according to the relationship $\tilde{\delta}(t)=(r(t)^3+R^3-r_f^3)^{1/3}-r(t)$ (which follows from the approximate volume conservation). For example, for $R=40$ nm, $r_f=34$ nm, and $r(t)=80$ nm, we obtain $\tilde{\delta}=1.26$ nm which is just three atomic layers. The thickness of the liquid shell cannot be smaller than the size of an atom, thus the shell will break into small sectors [Fig. 1(b)]. This may happen for larger thickness as well, due to possible heterogeneity in velocity and thickness. The next layers of the initial liquid drop will be separated from the drop as soon as tensile pressure reaches the value necessary for the fracture. Since tensile pressure without the fracture significantly exceeds the critical value $|p_c|$ (Figs. 6–8 and 10), we can conclude that the thickness of each subsequent separated liquid shell is on the order of one to several atomic sizes.

Thus, the tensile pressure disperses Al droplets into small (several atomic sizes) clusters which travel with high velocity (100–250 m/s). If they hit the oxidizer, a portion will penetrate it, some will spread over the surface and react, and a fraction will reflect and react with the next oxidizer particle. Al clusters may also react with oxygen (and nitro-

gen) in the air, with Teflon which starts to decompose at 825 K, with gaseous MoO_3 which starts to sublimate at 973 K, or some other oxidizer.

IV. SUPPORTING EXPERIMENTAL DATA

It is not currently possible to directly determine the reaction mechanism and to observe the melt dispersion mechanism. In this section we present macroscale experimental observations that support the melt dispersion mechanism.

(a) For each ultimate strength, σ_u, and the temperature at which the oxide film was formed, T_0, there is the critical value of M below which the entire particle melts ($f_f=1$) before the oxide shell fracture (Fig. 3). For this range of M, pressure in the Al is high enough (at least higher than 1 GPa) to cause cavitation. Thus, the melt dispersion mechanism will operate providing maximum possible mixing, oxidation rate, the flame front velocity, and energy release. According to this mechanism, one cannot expect an essential difference in the mixing of components and oxidation rate of particles for M smaller than this critical value. Currently, ignition delay time, t_{ig}, and the flame front velocity, C, are the major measurable parameters which characterize MICs combustion behavior. In our recent experiments for $Al+MoO_3$ MIC,[3] the flame propagation rate is approximately the same (950 m/s) for the Al nanoparticles with an average radii of $\tilde{R}=22$ and 40 nm and reduces for particles with a radii of $\tilde{R}=55$ and 60.5 nm ($1.8\leq\delta\leq2.0$ nm) (Fig. 3). In our other experiments,[5] laser induced ignition time delays are in the range of 12.4–25.5 ms for $\tilde{R}=(8.7-101)$ nm and ($1.8\leq\delta\leq7.7$ nm) and grows to 6.039 s for $\tilde{R}=20$ μm (Fig. 3). In Fig. 3, dimensionless normalized flame velocity, $\tilde{C}=C/(1\ \mathrm{km/s})$, from experiments,[3] and the ignition time delay $\tilde{t}_{ig}/(100\ \mathrm{ms})$ from experiments[5] are plotted versus M and superposed on the $f_f(M)$ curves. Note that the magnitudes of $\tilde{C}$ and $\tilde{t}_{ig}$ are irrelevant in the current discussions. The following results are important:

(1) Both $\tilde{C}$ and $\tilde{t}_{ig}$ are independent of M below some critical M which corresponds to the prediction of the theory.
(2) Despite the different and wide ranges of the particle radii and shell thicknesses in the experiments, critical values of M for $\tilde{C}$ ($M_c=19$) and for $\tilde{t}_{ig}$ ($M_c=17$) are practically the same. This means that $M=R/\delta$ (rather than R and δ separately) characterizes the reactivity of the thermites, which is in agreement with our theory. Also, the fact that two completely different parameters confirm the independence of the thermite reactivity of M provides an additional plausibility to our results.
(3) The maximum oxide thickness for which the independence of the ignition time delay was found in experiments was $\delta=7.7$ nm.[5] This means that the oxide shell of such a thickness possesses the required strength and breaks fast enough to ensure the conditions for the melt dispersion mechanism.
(4) The temperature at which the oxide shell formed, T_0, although not known exactly, was close to 300 K. According to Fig. 3(a), the complete melting before the fracture for this T_0 (consequently, independence of the reactivity of M) corresponds to $\sigma_u=\sigma_{\mathrm{th}}=11.33$ GPa, i.e., to the theoretical strength. Results of the items 3 and 4 will be used below to estimate the maximum particle radius for which the melt dispersion mechanism can be expended. The above results support our theory.

(b) In experiments,[29] the mean distance of reaction propagation from a single laser-ignited Al particle embedded in nitrocellulose was considered as a measure of combustion behavior. When the thermal explosion mechanism was dominant, an increase in the oxide shell thickness leading to a decrease in M from 11.1 to 4.2 did not increase reaction propagation distance. This is consistent with the melt dispersion mechanism and our experiments[3,5] since in both cases $M<19$ (Fig. 3). It also provides an alternative to t_{ig} and C as a measure of combustion behavior and shows the independence of combustion behavior on M below some critical M.

We cannot use the data from Ref. 29 for 100 ps pulse ignition because that initiation phenomena is related to a completely different regime (shock propagation mechanism and much higher temperatures leading to evaporation rather than melting). However, the fact that the increase in the oxide shell thickness increases pressure in Al is consistent with the strength model [Eq. (1) and fracture criterion].

Usually, an initial oxide layer was considered deadweight because it does not participate in reaction and is a heat sink. One of the main conclusions in Ref. 29 is that for heating rates of 10^{14} K/s leading to the detonation regime, the oxide shell plays an important positive role since its increase leads to an increase in reaction propagation distance, probably due to pressure increases within the Al core. For much lower heating rates and for thermal explosion oxidation mechanism, it was concluded in Ref. 29 that the oxide shell is deadweight, since an increase in oxide thickness leading to a decrease in M from 11.1 to 4.2 did not increase reaction propagation distance. It follows from the melt dispersion mechanism and experiments in Refs. 3 and 5 that even for the thermal explosion oxidation regime and $M>19$, increase in oxide shell thickness (or decrease in M) increases Al reactivity.

(c) Damage of the oxide shell acts to suppress the melt dispersion mechanism (since it reduces the strength of the shell and causes localized fracture rather than spallation). However, the damage promotes the traditional diffusion oxidation mechanism (since it provides additional channels for diffusion). Pressing MICs pellets in a die has to damage the oxide film. That is why the flame propagation velocity is expected to decrease with the sample density for MICs and grow for traditional micron size thermites. Such trends have been observed in our experiments.[11] Note that we can use data from[11] up to 50%–55% of theoretical maximum density, because for larger compaction similar trends may be related also to other processes (for example, suppressed gas convection). Also a flame rate less than 10 m/s may not provide a sufficient heating rate for the operation of the melt dispersion mechanism. On the contrary, vibrational compaction of MICs without applying the load should not damage the shell, thus the melt dispersion mechanism should not be sup-

pressed. This is confirmed in our experiments:[3] Vibrational compaction leading to the change in mass density in the range of 5%–10% of theoretical maximum density did not significantly change the flame velocity.

(d) Let us consider an ellipsoidal penny-shaped particle that mimics a nanoflake. It has two semiaxes b and $R \gg b$. It is easy to show that the maximum hoop stress is in the circular section of radius R is evaluated as $\sigma_h^{\max} \simeq -pR/(2\delta)$. The minimum hoop stress is in the elliptic section, $\sigma_h^{\min} \simeq -p\pi b/(4\delta)$, and is much smaller in magnitude. Consequently, simultaneous fracture and spallation of the entire oxide film is impossible. Fracture takes place along the circular section of radius R when the fracture criterion, $-\sigma_h^{\max} = \sigma_u$, is satisfied. That means that pressure in the melt is $p = 2\sigma_u \delta/R$ [similar to Eq. (7) for large spherical particles]. Usually nanoflakes have sizes in the range of $b = 10-100$ nm and $R = 10-100$ μm.[10] Consequently, pressure in the melt at the instant of nanoflake fracture has the same magnitude as in micron size particles with $R \gg \delta$. Thus, based on the melt dispersion mechanism, nanoflakes react similar to micron size particles; at the same time, traditional wisdom (higher reactivity for nanosize particle and large surface to volume ratio) would suggest at least similar reactivity for nanospherical and nanoflake particles. Experiments in Ref. 10 demonstrate that nanoflakes did not produce higher flame propagation velocity than micron spherical particles, consistent with the melt dispersion mechanism theory.

(e) We compressed a thin layer of nano Al powder between two steel pistons and then produced a large shear by rotating one of the pistons back and forth by 101^0. Total force was 1000 lbf and the piston diameter was 7.385 cm. The averaged pressure was 1 MPa. However, local pressure cannot be determined with reasonable accuracy, because we cannot exclude direct touching between pistons over some area. Such a process transformed some spherical particles into ellipsoidal flakes and also has to damage their oxide shells. Scanning electron microscopy (SEM) demonstrated that some small particles remain spherical and unchanged, while relatively large particles transformed to flakes and conglomerated.

The Al and MoO_3 powders were combined with approximately 90 ml of Hexane and sonicated with a sonic wand immersed in the slurry. A cycle of 10 s on 10 s off for a total of 70 s on was used to keep the temperature of the slurry relatively constant. Sonication destroyed the Al conglomerates. After sonication of deformed Al powder mixed with MoO_3 powder, SEM pictures do not show any difference in conglomeration in comparison with undeformed Al powder (Fig. 11).

An open channel combustion experiment with $Al+MoO_3$ mixtures (similar to that described in Refs. 3 and 4) was conducted. Three experiments have been performed for damaged and undamaged Al particles. We observed that the flame propagation rate $C = 342 \pm 11$ m/s for undamaged spherical particles and $C = 174 \pm 7$ m/s for damaged particles. This result supports the melt dispersion mechanism.

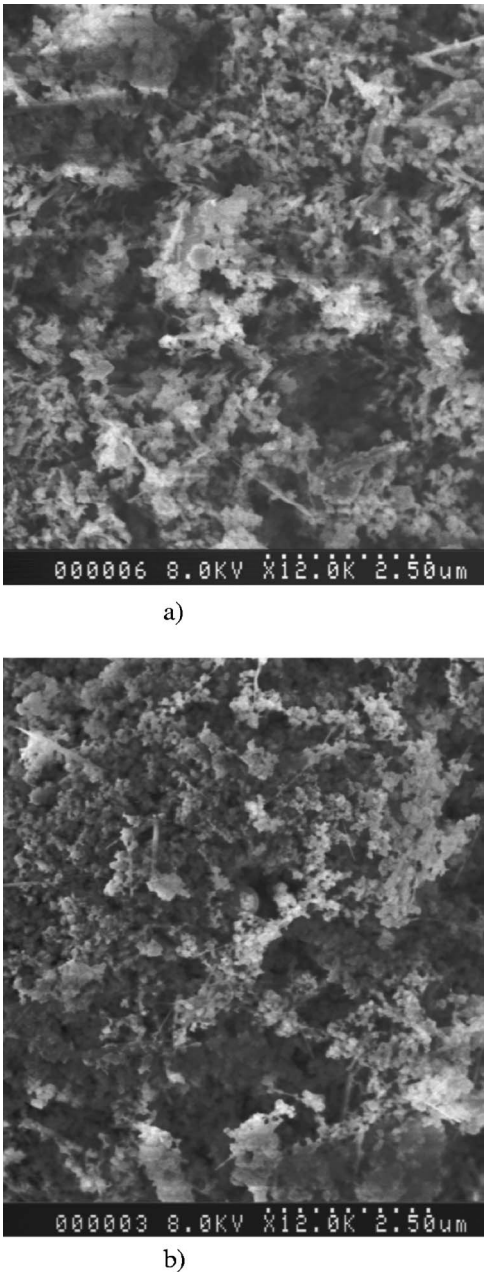

FIG. 11. Scanning electron microscopy images of the Al and MoO_3 mixtures after sonication. (a). Undamaged Al. (b). Damaged Al. No visible difference in conglomeration is observed between deformed and nondeformed structure.

V. CONDITIONS FOR THE MELT DISPERSION MECHANISM AND METHODS TO CONTROL THEM

A. Main conditions

The main conditions for the optimal dispersion of the spherical Al particle are:

(1) The aluminum core has to completely melt before the oxide shell fracture and spallation. If we know the ultimate strength of the oxide shell, σ_u, and the temperature at which the oxide film was formed, T_0, then using Fig. 3 we can determine the maximum value M for which the entire particle melts. As we discussed in Sec. IV, $T_0 = 300$ K and comparison with experiments [Fig. 3(a)] suggests that $\sigma_u = \sigma_{\text{th}} = 11.33$ GPa. The maximum value of $M_m = 20$ corresponds to

complete melting [Fig. 3(a)]. For $T_0=450$ K we obtain $M_m=29$; for $T_0=600$ K one gets $M_m=52$; and for $T_0=785$ K Al melts for arbitrarily large M. The condition for almost homogeneous temperature in the Al core necessary for the complete melting is met for core radius $R<9.12$ μm (see Appendix A), i.e., it is not restrictive.

(2) The oxide shell fracture has to occur simultaneously in the entire shell; the oxide shell fracture time has to be smaller than the acoustic time ($t_s<t_p$). These conditions can be fulfilled for a thin, amorphous, defect-free, or nanocrystalline oxide shell, and only during fast heating. Any defect will cause a localized fracture near it rather than a homogeneous fracture in the whole oxide shell, which may lead to the flow of the liquid through the hole (similar to Ref. 26) rather than dispersion of the droplet. Also, defects cause reduction in the ultimate strength σ_u and consequently in the pressure in the droplet by one to several orders of magnitude. This will reduce proportionally the tensile pressure in the liquid and may prevent cavitation. Thus, the oxide shell thickness has to be limited to 2–10 nm; at least for $\delta=7.7$ nm, experimental results on ignition time delay[5] are consistent with the melt dispersion mechanism. Taking $\delta=7.7$ nm and $M_m=20$ for $T_0=300$ K results in $R=144$ nm.

(3) Pressure in the Al core at the instant of oxide film fracture has to be approximately equal to the cavitation pressure. More precisely, we will use the following conditions to determine the required pressure p_0 and the oxide shell fracture time $\bar{t}_s$. We will consider $\bar{t}=1$ as the best time instant for cavitation (since particle velocity is from the center everywhere and pressure in the entire central part of the sphere, $\bar{p}_m$, is constant and negative). Then from the cavitation condition $\bar{p}_m=\bar{p}_c$ we obtain constrains Eqs. (20) and (21) with the equality sign. The equality in Eq. (21) can be resolved for the pressure p_0 required for cavitation

$$p_0=\frac{-p_c\bar{t}_s+p_f}{1-\bar{t}_s}. \tag{22}$$

From the one side, the smaller $\bar{t}_s$ is, the smaller pressure p_0 is required for cavitation. From another side, since $\bar{r}_m=\bar{t}_s$, decrease in $\bar{t}_s$ decreases the portion of the Al sphere where cavitation criterion is satisfied. If we accept $\bar{r}_m=0.5$, then Eq. (22) simplifies to

$$p_0=-p_c+2p_f. \tag{23}$$

This cavitation criterion is met in the region $\bar{r}_m=\bar{t}_s\leq 0.5$. For the above obtained parameters ($M=20$, $\sigma_u=11.33$ GPa, and $\delta=7.7$ nm), the pressure in Al during complete melting and oxide fracture is $p_0=1.16$ GPa [see Fig. 2(a) and Eq. (1)], which for $p_f=0.05$ GPa corresponds to $-p_c=1.06$ GPa [Eq. (23)]. Taking $-p_c=0.1$ GPa one can satisfy Eq. (22), for example, for $p_0=0.2$ GPa and $\bar{r}=\bar{t}_s=0.86$.

(4) The liquid dispersion mechanism can operate if there is enough free space around Al particles. High flame velocity was observed for a loose mixture of Al+MoO_3 or Al+Fe_2O_3 only;[1–4] for compacted tablets, flame rate is much slower and even decreases with Al particle radius[5] (presumably due to the decrease of the einitial ratio of Al to alumina mass).

B. Some methods to promote the melting dispersion mechanism

Based on our analysis, we can predict several ways to expand the melt dispersion mechanism for larger particles.

(1) The main limitation is currently related to the condition that the entire particle melts before fracture. As we found above, for currently achievable parameters ($\delta=7.7$ nm, $M_m=20$, and $T_0=300$ K) we obtain $R=144$ nm. Increase in δ will increase R proportionally. Progress here is related to the development of a technology to produce thicker defect free films. Even if $\delta=20$ nm and consequently $R=400$ nm can be achieved, it may prove difficult to fracture the entire film simultaneously and spallate it.

We predict that increasing the temperature at which an initial oxide shell was formed, T_0, may increase the particle size for which the melt dispersion mechanism is operative (Fig. 3). Thus, for $T_0=450$ K one gets $M_m=29$ and for $T_0=600$ K we obtain $M_m=52$; for $\delta=10$ nm this results in $R=290$ nm and $R=520$ nm, respectively. The pressure in Al core just before fracture for these cases is 0.72 and 0.44 GPa, correspondingly, which is sufficient to cause cavitation.

For $T_0=785$ K Al melts for arbitrary large M (with limitation on the temperature variation along the radius). Thus the value M will be determined from the condition (23) that the created pressure in Al can cause cavitation. Substituting in the cavitation condition (23), Eq. (7) for p_0 (for $\Gamma_1=\Gamma_2$), and $p_f=2\Gamma/R+p_g$(GPa), we obtain

$$M=\frac{2\sigma_u}{-0.5p_c+p_g}. \tag{24}$$

The interface energy does not contribute to Eq. (24) but this is because of our choice that $\bar{t}=0.5$ only. For $p_c=-0.1$, $p_g=0.01$, and $\sigma_u=11.33$ GPa, one obtains $M=338$; for $p_c=-0.01$ and the same p_g and σ_u, one obtains $M=1133$; for $\delta=10$ nm these values of M result in $R=3.38$ μm and $R=11.3$ μm, respectively. Note that the pressure in the Al core for these two cases is 0.08 and 0.03 GPa, respectively.

There is, however, a limitation that for high T_0, a decohesion of oxide film will occur during the cooling from T_0 to room temperature [due to tensile pressure determined from Eq. (1) for $f=0$ and $T<T_0$]. This may lead to the fracture of the oxide film due to buckling[14] and oxidation of bare Al, so T_0 will be decreased and a defective film will be created.

(b) One more method that allows us to decrease internal stresses before melting (or before complete melting) and to guarantee complete melting before the oxide fracture is to synthesize nanoparticles with initial porosity. Using the plasticity theory,[15] one can derive a relationship between the equilibrium concentration of void and applied pressure $V_e=\exp(-1.5p/\sigma_y)$, where σ_y is the yield strength of Al. If initial porosity V_e^0 is greater than V_e, it will be reduced to V_e, otherwise it will not change. The difference $\Delta\varepsilon_v=(V_e-V_e^0)/3<0$ has to be added to ε_1^i in Eq. (3) which will reduce the pressure and hoop stresses. By tailoring initial porosity, one cannot only avoid a fracture before melting but also prescribe at which temperature above T_m the fracture will occur. This will allow the melt dispersion mechanism to occur at the optimal conditions, e.g., when oxidizer melts or

sublimates. Even a fracture of the alumina during phase transformation can be prevented due to initial porosity. However, phase transformation to the polycrystalline γ phase will create numerous defects reducing σ_u which may not allow the Al to reach pressure sufficient for cavitation.

(c) Mixing Al with some material with low (or even negative) thermal expansion coefficient or a material that undergoes a phase transformation with the reduction in volume can also prevent a fracture of the oxide shell before melting the Al for large particles.

(d) To ensure the fast heating rate for large particles, one can mix them with nanoscale particles ($R<40-100$ nm) that react according to the melt dispersion mechanism. Note that if nanosized particles provide the fast temperature increase above 2800–3600 K (for gas pressure in range 1–32 atm)[30,6] then the Al in the remaining micron sized particles will vaporize (and alumina will melt) and oxidize very fast in a gas state. As it was found previously in Ref. 31 mixing 30% micron scale particles with $\tilde{R}=2$ and 10 μm and 70% Al nanoparticles with an averaged radius $\tilde{R}=40$ nm ($R/\delta=8.3$) lead practically to the same flame propagation rate as 100% of Al nanoparticles. It is possible that only some portion of the micron size particles which ensure ignition and initiation of the flame propagation have to be mixed with nanoparticles. They produce a fast flame propagation rate which ensures a rapid heating rate in the remaining micron size particles.

(e) To locally reduce the surface energy of metallic particle, and consequently, reduce cavitation pressure, one may use a special alloying. Porosity in a fuel [considered in item (b)] may cause density fluctuations in the melt and seed the nucleation of cavitation.

(f) An alternative way to cause the dispersion of not only fuel particles but also of oxidizer particles is to fabricate them with inclusions of a material that gasifies (or explodes) at the prescribed temperature, fracturing solid (or liquid) fuel, and oxidizer particles. The case when the gasifying particles are an oxidizer within a fuel matrix or a fuel within an oxidizer matrix is optimal. This mechanism is independent of the existence and fracture of the initial oxide shell and heating rate and may work for much larger particles ($10-100$ μm). They, however, have to be mixed with nanosized particles to ensure fast initial heating, if the fast flame propagation is a goal. The closeness of sublimation temperature of inclusions to melting or sublimation temperature of fuel and oxidizer will also accelerate the oxidation.

C. Other cases when particle dispersion mechanism may be operative

There is a probability that the particle dispersion mechanism may operate at less restrictive conditions:

(a) When only part of the Al particle melts;
(b) when it melts and disperses simultaneously due to reduction in melting temperature in the tensile wave;
(c) when the solid particles disperse in a tensile wave;
(d) when melting occurs after one or several oxide fracture-healing cycles.

Allow fracture to occur at f slightly smaller than one. First, if a few *nm* solid spheres will remain after melt dispersion, they will melt and oxidize in the next few μs during further heating. If a significant part of the Al particle remains solid, it still can be dispersed for small initial particles, because pressure (and consequently tensile stresses in an unloading wave) in small particles may be high enough (Figs. 6–10) to disperse even solid particles close to the melting point. Note that impedances, $Z=\rho c$, of solid and liquid Al near the melting points are close [based on Table I, $Z^s=1.346\times10^7$ and $Z^m=9.914\times10^6$ kg/(m^2c)] and only $(Z^m-Z^s)^2/(Z^m+Z^s)^2\times100=2.3\%$ of energy is reflected.

Also, tensile stresses reduce the melting temperature by 55 K/GPa (Ref. 24) to 65 K/GPa,[32] thus melting and melt dispersion may occur simultaneously. For larger particles and lower pressures, only the melted part and near surface area of the remaining particle will be oxidized during the time the flame front passes through it; so the solid core will not contribute significantly to the acceleration of the flame. Also, tensile pressure in an unloading wave develops after it travels some distance. If, e.g., the cavitation criterion for liquid Al is fulfilled at $\bar{r}=0.75$, then the oxide has to be broken at the value of f not smaller than $f=1-\bar{r}^3=0.58$.

VI. CONCLUDING REMARKS

To summarize, a melt dispersion mechanism of fast reaction of spherical Al nanoparticles initially covered by a thin amorphous oxide shell during fast heating was suggested and justified theoretically and experimentally. Despite the indeterminacy of some material parameters and simple models, there is a broad range of parameters for which the suggested mechanism is operative; we cannot imagine at this point any other possible mechanism. This mechanism transforms Al particles with diameters on the order of tens of nanometers covered by oxide film into nanometer sized bare liquid clusters. Oxidation (or any other reaction) of such clusters is not limited by diffusion (in contrast to traditional mechanisms). Ignition and flame propagation are no longer controlled by the chemical reaction. For nanoflake or other significantly asymmetric geometries, this mechanism cannot operate, which corresponds to experiments. Below some critical particle size for which the entire particle melts and the melt dispersion mechanism operates, oxidation rate, ignition delay time, and flame velocity are to be independent of the particle size, which also corresponds to experiments.[3,5] Damage of the oxide shell suppresses the melt dispersion mechanism and promotes traditional diffusive oxide growth, in accordance with our experimental findings. We also found physical parameters, controlling the melt dispersion mechanism which can be used to expand the operation region of this mechanism. Thus, increasing the temperature at which the initial oxide was formed, T_0, creation of initial porosity in Al, mixing of Al with a material with a low (or even negative) thermal expansion coefficient, or with a phase transformation accompanied by volume reduction, alloying Al to decrease the cavitation pressure, mixing of nano and micron

particles, and introducing gasifying or explosive inclusions in any fuel and oxidizer follows from our theory. These predictions can be used for experimental verification in the near future.

A similar mechanism is expected for nitridation and fluorination of Al. We do not anticipate that fluorination will chemically reduce the oxide shell thickness during the 10 μs ignition time; otherwise, the initial oxide shell thickness will have to be increased accordingly. This mechanism may also be tailored for Ti (T_m=1933 K) and Mg fuel (T_m=922 K), if they will be subjected to a high heating rate. The difference in thermal expansion coefficients for Ti and its oxide is very small and does not cause fracture before T_m.[13] Change in volume during phase transformation is also small (0.1%–0.3%);[14] transformation may not occur at very fast heating. Fast initial heating can be provided by the mixing of some portion of Ti and its oxidant with Al. The behavior of Mg may be very similar to Al.

Attempts to directly confirm the melt dispersion mechanism should be made, both experimentally and using molecular dynamics simulation (for nanosize particles). Also, much more detailed modeling of this mechanism will require significant advances in scale-dependent nano and microscale nonlinear elasticity, plasticity (in the presence of porosity) and dynamic fracture of solids, nonlinear nano fluid dynamics, coupled to oxidation kinetics, thus promoting multidisciplinary approaches.

ACKNOWLEDGMENTS

V.I.L. and M.L.P. acknowledge the Office of Naval Research Grant No. N000140710318 with Judah Goldwasser as Program Officer. We also acknowledge the LANL contracts (Contract Nos. 13720–001–05-AH and 31553–002–06) and NSF grants (Grant No. CMS-0555909 with Ken Chong as Program Director) (V.I.L.), the Joint Munitions Program (B.W.A. and S.F.S.), with Sherry Bingert as Program Manager and the Army Research Office Grant No. W911NF-04–1-0217 (M.L.P.), as well as the assistance of D. Osborn and D. Prentice (T.T.U.).

APPENDIX A: THERMAL CONDUCTIVITY

Let us consider the heating of an Al spherical particle with radius R. Let the surface temperature of the particle vary from T_r=300 K to the final $T_f \simeq 1000$ K during time t_f=10 μs (i.e., while flame front passes through it). The equation of thermal conductivity in spherical coordinates is

$$\frac{\partial T}{\partial t} = a\left(\frac{\partial^2 T}{\partial r^2} + \frac{2}{r}\frac{\partial T}{\partial r}\right), \tag{A1}$$

where a is the thermal diffusivity. Due to symmetry, at the center of the sphere $\partial T(0,t)/\partial r=0$. For very small radius R, assume the temperature gradient along the radius is small (which will be proven below) and use the first two terms of Taylor's series expansion, $T(r,t)=A+Br^2$, which satisfy conditions at the center of sphere. The Laplacian in the right-hand side of Eq. (A1) is equal to $6B$. For $t=t_f$, $T(0,t_f)=A$ and $T(R,t_f)=A+BR^2$, thus $B=(T(R,t_f)-T(0,t_f))/R^2$. Approximating $\partial T/\partial t \simeq (T_f-T_r)/t_f$ and substituting all terms in Eq. (A1), one obtains

$$T(R,t_f) - T(0,t_f) \simeq (T_f - T_r)R^2/(6t_f a). \tag{A2}$$

Taking $a=9.71\times10^{-5}$ m^2/s for Al and the above data for all parameters, we obtain that temperature at the center is lower than at the surface by less than 1 K for $R<2.88$ μm (or less than 10 K at $R<9.12$ μm) and will be considered homogeneous. Thus, thermal conductivity is not a limiting process in our study.

APPENDIX B: STRESSES IN TWO LAYERED SPHERE

Let us derive equations for the pressure and hoop stresses in a two-layer sphere with an external sphere radius $\tilde{R}$ and internal sphere radius R, using the elasticity theory. An analytical solution can be presented in the form[15]

$$\begin{aligned} u_j &= -(A_j r + B_j/r^2), \\ p_j &= -(3K_j(A_j - \varepsilon_j^i) - 4G_j B_j/r^3), \\ \sigma_{hj} &= -(3K_j(A_j - \varepsilon_j^i) + 2G_j B_j/r^3). \end{aligned} \tag{B1}$$

Here u is the radial displacement, p and σ_h are the radial and hoop stresses, $j=1$ is for the internal sphere (Al) and $j=2$ is for the external layer (oxide shell), r is the spherical coordinate and constants A_j and B_j are to be determined from the boundary conditions and conditions at $r=R$. All designations are the same as in Sec. II. Negative signs in Eq. (B1) are due to the convention that compressive stresses and strains are positive. Since stresses and displacements have to be finite at $r=0$, one obtains $B_1=0$; thus, radial and hoop stresses in an internal sphere are equal to the mean pressure and are uniform. Displacement continuity across the interface $r=R$, the jump condition for traction across the interface $r=R$ and the boundary condition at the external surface $r=\tilde{R}$ result in three linear algebraic equations

$$u_1(R) = u_2(R);\ \ p_1(R) = p_2(R) + 2\Gamma_1/R;\ \ p_2(\tilde{R}) = 2\Gamma_2/R + p_g, \tag{B2}$$

for determination of A_1, A_2, and B_2. Substituting the derived expressions for A_1, A_2, and B_2 in Eqs. (B1) results in Eqs. (1) and (2) for the pressure in the internal sphere and the hoop stresses in the shell at $r=R$.

APPENDIX C: WAVE PROPAGATION

Spherical waves in liquid or gas can be described by the following equations:[33]

$$\frac{\partial^2 f}{\partial^2 t} = c^2 \frac{\partial^2 f}{\partial^2 r}, \tag{C1}$$

$$\varphi := f/r;\ \ p = -\rho\frac{\partial \varphi}{\partial t};\ \ v = \frac{\partial \varphi}{\partial r}. \tag{C2}$$

The following problem will be considered: A sphere of radius R is initially in equilibrium under applied external pressure p_0. The purpose is to determine the evolution of the pressure, p, and particle velocity, v, after a fast change in

external pressure $p_{ex}(t)$, in particular under unloading down to some final pressure p_f. For this problem consider unloading and the first wave reflected from the center only, because for larger time the solid oxide layer may be again formed at the external surface of the liquid drop (see Sec. III). The method of propagating waves and the Dalambert equation[34] is used to solve this problem. The initial and boundary conditions are

$$p(r,0)=p_0;\ \ v(r,0)=0;\ \ v(0,t)=0;\ \ p(R,t)=p_{ex}(t). \tag{C3}$$

These conditions will be transformed to the conditions for function f. A solution to this problem can be obtained by combining two problems:

(1) A solution to the problem with zero boundary conditions for f (or p), i.e., a free oscillation problem:

$$p(r,0)=p_0;\ \ v(r,0)=0;\ \ v(0,t)=0;\ \ p(R,t)=0. \tag{C4}$$

This problem can be solved in two steps:

(1a) A solution for an infinite sphere for which the boundary condition $p(R,t)=0$ is neglected;

(1b) a solution for a finite sphere that satisfies the boundary condition $p(R,t)=0$;

(2) propagation of the boundary regime

$$p(r,0)=0;\ \ v(r,0)=0;\ \ v(0,t)=0;\ \ p(R,t)=p_{ex}(t). \tag{C5}$$

First, find scaling rules for the pressure and velocity using dimensional analysis. The solutions depend on the following dimensional parameters: p_0, ρ, c, and R. It follows from Eq. (C2) for pressure that function φ can be presented as $\varphi=(p_0R/\rho c)\bar{\varphi}$, where the bar designates a dimensionless function. Then Eq. (C2) results in

$$f=\frac{p_0R^2}{\rho c}\bar{f};\ \ p=p_0\bar{p};\ \ v=\frac{p_0}{\rho c}\bar{v}. \tag{C6}$$

Note if one would start with Eq. (C2) for velocity, one obtains an incorrect result: $\varphi=cR\bar{\varphi}$, $f=cR^2\bar{f}$, $p=\rho c^2\bar{p}$, and $v=c\bar{v}$. This means that dimensional analysis does not give an unambiguous result; however, Eq. (C6) is confirmed by the direct solution of Eqs. (C1)–(C3). Dimensionless functions $\bar{f}$, $\bar{\varphi}$, $\bar{v}$, and $\bar{p}$ depend on dimensionless coordinate $\bar{r}:=r/R$ and time $\bar{t}:=t/t_p$, where we define an acoustic time $t_p:=R/c$ during which the wave propagates from the surface to the center of the sphere.

Problem 1a. A solution of the wave equation can be presented in the form

$$f_h(r,t)=q_1(r+ct)+q_2(r-ct), \tag{C7}$$

where q_1 and q_2 are some functions. Since the function φ_h is finite at $r=0$, then $f_h(0,t)=0$. This implies $q_1(ct)=-q_2(-ct)$ and

$$f_h=q(r+ct)-q(ct-r);\ \ \varphi_h=\frac{q(r+ct)-q(ct-r)}{r}. \tag{C8}$$

The initial condition $v(r,0)=\partial\varphi(r,0)/\partial r=0$, results in $\varphi(r,0)=$const. Since it follows from Eq. (C8) that $\varphi(0,t)=0$, and in particular, $\varphi(0,0)=0$, then $\varphi(r,0)=0$ and $q(r)=q(-r)$. Since the derivative of the even function is the odd function, then $dq(r)/dr=-dq(-r)/dr$. Another initial condition

$$p(r,0)=-\rho\frac{\partial\varphi(r,0)}{\partial t}=-\frac{\rho c}{r}\left(\frac{dq(r)}{dr}-\frac{dq(-r)}{dr}\right)$$
$$=-\frac{2\rho c}{r}\frac{dq(r)}{dr}=p_0 \tag{C9}$$

results in

$$q=-\frac{p_0}{4\rho c}r^2+\text{const}. \tag{C10}$$

Substituting this expression in Eq. (C8), one obtains

$$f_h=-\frac{p_0tr}{\rho}. \tag{C11}$$

This solution corresponds to constant $p=p_0$ and $v=0$, i.e., there are no oscillations in an infinite sphere.

Problem 1b. To modify the above problem for a finite sphere and consider the boundary condition $p(R,t)=0$ which corresponds to $f_h(R,t)=0$, we have to represent f_h in the form[34]

$$f_h=0.5(\Phi(r+ct)+\Phi(r-ct))+\frac{1}{2c}\int_{r-ct}^{r+ct}\Psi(\alpha)d\alpha, \tag{C12}$$

where Φ and Ψ are periodic functions with period $2R$ and are odd with respect to the points $r=0$ and $r=R$ and determined by the initial conditions at $0\le r\le R$

$$f_h(r,0)=\Phi(r);\ \ \frac{\partial f_h(r,0)}{\partial t}=\Psi(r). \tag{C13}$$

Using Eq. (C11), we obtain $\Phi=0$ and $\Psi=-p_0r/\rho$ at $0\le r\le R$. Since Ψ is an odd function with respect to the point $r=0$, Ψ has the same expression for $-R\le r\le R$. If we introduce the unit step function on the interval $[a,b]$ (which is equal to 1 on the interval $[a,b]$ and to 0 outside the interval $[a,b]$) by the equation $U(a,b)=H(\alpha-a)H(b-\alpha)$, where H is the Heaviside unit step function [$H(\alpha-a)=1$ for $\alpha\ge a$ and $H(\alpha-a)=0$ for $\alpha<a$], then we can continue function Ψ periodically (Fig. 5):

$$\Psi(\alpha)=-\frac{p_0}{\rho}[\alpha U(-R,R)+(\alpha-2R)U(R,3R)$$
$$+(\alpha+2R)U(-3R,-R)]\ \text{ for }\ -3R\le\alpha\le 3R, \tag{C14}$$

or using dimensionless form

$$\Psi(\alpha)=\frac{p_0R}{\rho}\overline{\Psi}(\overline{\alpha}),$$

$$\overline{\alpha}:=\alpha/R, \tag{C15}$$

$$\overline{\Psi}(\overline{\alpha}):=-[\overline{\alpha}U(-1,1)+(\overline{\alpha}-2)U(1,3)+(\overline{\alpha}+2)U(-3,-1)]$$
$$\text{for } -3\le\overline{\alpha}\le 3.$$

For unloading and reflected waves, $0\le r\le R$ and $0\le ct\le 2R$; then $0\le r+ct\le 3R$ and $-2R\le r-ct\le R$. That is why the interval $-3R\le\alpha\le 3R$ is sufficient for our purposes but the function Ψ can be easily periodically continued by adding the terms $(\alpha-(n+1)R)U(Rn,R(n+2))$ with positive and negative integers n. Thus, function Ψ represents a straight line in the interval $[-R,R]$ passing through zero which is periodically continued along the α axis (Fig. 5). Then, according to Eq. (C12)

$$f_h=G(r+ct)-G(r-ct),$$

$$G(\alpha)=\frac{1}{2c}\int_0^{\alpha}\Psi(\xi)d\xi \tag{C16}$$

$$=-\frac{p_0}{4\rho c}[U(-R,R)\alpha^2+U(R,3R)(\alpha-2R)^2+U(-3R,-R)(2R+\alpha)^2],$$

or using dimensionless form

$$f_h=\frac{p_0R^2}{\rho c}\bar{f}_h,$$

$$\bar{f}_h:=\overline{G}(\bar{r}+\bar{t})-\overline{G}(\bar{r}-\bar{t}), \tag{C17}$$

$$\overline{G}(\overline{\alpha})=\frac{1}{2}\int_0^{\overline{\alpha}}\overline{\Psi}(\xi)d\xi$$

$$=-\frac{1}{4}[U(-1,1)\overline{\alpha}^2+U(1,3)(\overline{\alpha}-2)^2+U(-3,-1)(2+\overline{\alpha})^2].$$

Again, terms $0.5(\alpha-(n+1)R)^2U(Rn,R(n+2))$ can be added for further periodic continuation. Using Eq. (C2) we obtain for pressure and particle velocity

$$p_h=-\frac{\rho}{2r}(\Psi(r+ct)+\Psi(r-ct))=\frac{p_0}{\bar{r}}\bar{p}_h;$$

$$\bar{p}_h:=-\frac{1}{2}(\overline{\Psi}(\bar{r}+\bar{t})+\overline{\Psi}(\bar{r}-\bar{t})), \tag{C18}$$

$$v_h=\frac{p_0}{\rho c}\frac{\partial(\bar{f}_h/\bar{r})}{\partial\bar{r}}=\frac{p_0}{\rho c\bar{r}}\left[\frac{1}{2}(\overline{\Psi}(\bar{r}+\bar{t})-\overline{\Psi}(\bar{r}-\bar{t}))-\frac{\bar{f}_h}{\bar{r}}\right]. \tag{C19}$$

Problem 2. Let us consider propagation of the boundary regime $p(R,t)=p_{ex}(t)$. Using Eq. (C2), we obtain the corresponding boundary condition for the function f_b:

$$f_b(R,t)=f_{ex}(t)=-(R/\rho)\int_0^t p_{ex}(\tau)d\tau=\frac{p_0R^2}{\rho c}\bar{f}_{ex}(\bar{t}),$$

where

$$\bar{f}_{ex}(\bar{t}):=-\int_0^{\bar{t}}\bar{p}_{ex}(\tau)d\tau,\quad \bar{p}_{ex}:=p_{ex}/p_0.$$

Then if we are interested in propagation of the boundary regime to the center of the sphere and one reflection from the center, the propagating and reflecting waves have to be combined

$$f_b=f_{ex}[t-(R-r)/c]-f_{ex}[t-(R+r)/c]=\frac{p_0R^2}{\rho c}\bar{f}_b,$$

$$\bar{f}_b:=\bar{f}_{ex}(\bar{t}+\bar{r}-1)-\bar{f}_{ex}(\bar{t}-\bar{r}-1). \tag{C20}$$

Generalization for an arbitrary number of reflections from the center and free surface of the sphere can be obtained in a standard way.[34] Then using Eq. (C2) we obtain

$$p_b=-\frac{p_0}{\bar{r}}\frac{\partial\bar{f}_b}{\partial\bar{t}},\quad v_b=\frac{p_0}{\rho c}\frac{\partial(\bar{f}_b/\bar{r})}{\partial\bar{r}}. \tag{C21}$$

Expressions for the pressure and velocity can be simplified using the definition of f_{ex}

$$p_b=\frac{1}{\bar{r}}(p_{ex}[t-(R-r)/c]-p_{ex}[t-(R+r)/c])$$

$$=\frac{p_0}{\bar{r}}(\bar{p}_{ex}[\bar{t}+\bar{r}-1]-\bar{p}_{ex}[\bar{t}-\bar{r}-1]), \tag{C22}$$

$$v_b=-\frac{p_0}{\rho c\bar{r}}\left[\bar{p}_{ex}(\bar{r}+\bar{t}-1)+\bar{p}_{ex}(\bar{r}-\bar{t}-1)+\frac{\bar{f}_b}{\bar{r}}\right]. \tag{C23}$$

The complete solution of the problem is a combination of two solutions

$$p=p_h+p_b;\quad v=v_h+v_b. \tag{C24}$$

[1] B. W. Asay, S. F. Son, J. R. Busse, and D. M. Oschwald, Propellants, Explos., Pyrotech. **29**, 216 (2004).
[2] S. F. Son, W. C. Danen, B. S. Jorgensen, B. W. Asay, J. R. Busse, and M. L. Pantoya, in *Defense Applications of Nanomaterials*, edited by A. W. Miziolek, S. P. Karna, J. M. Mauro, and R. A. Vaia, ACS Symposium Series 891, 2005, Chap. 16, pp. 227–240.
[3] B. S. Bockmon, M. L. Pantoya, S. F. Son, B. W. Asay, and J. T. Mang, J. Appl. Phys. **98**, 064903 (2005).
[4] K. B. Plantier, M. L. Pantoya, and A. E. Gash, Combust. Flame **140**, 299 (2005).
[5] J. J. Granier and M. L. Pantoya, Combust. Flame **138**, 373 (2004).
[6] T. Bazyn, H. Krier, and N. Glumac, Combust. Flame **145**, 703 (2006).
[7] K. Park, D. Lee, A. Rai, D. Mukherjee, and M. Zachariah, J. Phys. Chem. B **109**, 729 (2005).
[8] E. Bergsmark, C. J. Simensen, and P. Kofstad, Mater. Sci. Eng., A **120**, 91 (1989).
[9] T. A. Bruzostowski and I. Glassman, in *Heterogeneous Combustion*, edited by H. G. Wolfhard, I. Glassman, and L. Green, Jr. (Academic, New York, 1964).

[10]B. Z. Eapen, V. K. Hoffmann, M. Schoenitz, and E. L. Dreizin, Combust. Sci. Technol. **176**, 1055 (2004).
[11]M. L. Pantoya and J. J. Granier, Propellants, Explos., Pyrotech. **30**, 53 (2005).
[12]V. I. Levitas, B. W. Asay, S. F. Son, and M. Pantoya, Appl. Phys. Lett. **89**, 071909 (2006).
[13]V. Rosenband and N. I. Vaganova, Combust. Flame **88**, 113 (1992).
[14]V. Rosenband, Combust. Flame **137**, 366 (2004).
[15]J. Lubliner, *Plasticity Theory* (Macmillan, New York, 1990).
[16]L. P. H. Jeurgens, W. G. Sloof, F. D. Tichelaar, and E. J. Mittemeijer, Thin Solid Films **418**, 89 (2002).
[17]A. L. Ramaswamy and P. Kaste, J. Energ. Mater. **23**, 1 (2005).
[18]S. Raju, K. Sivasubramanian, and E. Mohandas, Solid State Commun. **122**, 671 (2002).
[19]M. A. Trunov, M. Schoenitz, and E. L. Dreizin, Propellants, Explos., Pyrotech. **30**, 36 (2005).
[20]M. A. Trunov, M. Schoenitz, X. Zhu, and E. L. Dreizin, Combust. Flame **140**, 310 (2005).
[21]H. J. Frost and M. F. Ashby, *Deformation-Mechanism Maps* (Pergamon, New York, 1989).
[22]T. J. Campbell, R. K. Kalia, A. Nakano, P. Vashishta, S. Ogata, and S. Rodgers, Phys. Rev. Lett. **82**, 4866 (1999).
[23]T. J. Campbell, G. Aral, S. Ogata, R. K. Kalia, A. Nakano, and P. Vashishta, Phys. Rev. B **71**, 205413 (2005).
[24]Q. S. Mei, S. C. Wang, H. T. Cong, Z. H. Jin, and K. Lu, Acta Mater. **53**, 1059 (2005).
[25]J. Eckert, J. C. Holzer, C. C. Ahn, Z. Fu, and W. L. Johnson, Nanostruct. Mater. **2**, 407 (1993).
[26]A. Rai, D. Lee, K. Park, and M. Zachariah, J. Phys. Chem. B **108**, 14793 (2004).
[27]A. G. Merzhanov, Yu. M. Grigorjev, and Yu. A. Gal'chenko, Combust. Flame **29**, 1 (1977).
[28]Ya. B. Zeldovitch, Acta Physicochim. USSR **18**, 1 (1943).
[29]S. Wang, Y. Yang, H. Yu, and D. D. Dlott, Propellants, Explos., Pyrotech. **30**, 148 (2005).
[30]I. Glassman, *Combustion*, 3rd ed. (Academic, San Diego, California, 1996), Chap. 9.
[31]K. Moore, M. L. Pantoya, and S. F. Son, J. Propul. Power (in press).
[32]E. Yu. Tonkov, *High Pressure Phase Transformations. A Handbook* (Gordon and Breach, Philadelphia, 1992), Vol. 1, p. 24.
[33]L. D. Landau and E. M. Lifshitz, *Course of Theoretical Physics, Vol. 6, Fluid Mechanics* (Reed Educational and Professional Publishing, Oxford, 2000).
[34]A. N. Tychonov and A. A. Samarski, *Partial Differential Equations of Mathematical Physics* (Holden-Day, San Francisco, 1970).
[35]O. L. Anderson, *Equations of State of Solids for Geophysics and Ceramic Science* (Oxford University Press, Oxford, 1995), p. 362.
[36]D. C. Wallace, *Thermodynamics of Crystals* (Wiley, New York, 1972).
[37]V. E. Zinov'ev, *Handbook of Thermophysical Properties of Metals at High Temperatures* (Nova Science, New York, 1996), p. 140.
[38]P. M. Smith, J. W. Elmer, and G. F. Gallegos, Scr. Mater. **40**, 937 (1999).
[39]V. Sarou-Kanian, F. Millot, and J.-C. Rifflet, Int. J. Thermophys. **24**, 277 (2003).